Simultaneous multi-scale and multi-instrument observations of Saturn's aurorae during the 2013 observing campaign

Henrik Melin[a,b], S. V. Badman[c], T. S. Stallard[a], S. W. H. Cowley[a], U. Dyudina[j], J. D. Nichols[a], G. Provan[a], J. O'Donoghue[f], W. R. Pryor[g], K. H. Baines[d], S. Miller[e], J. Gustin[h], A. Radioti[h], C. Tao[i], C. J. Meredith[a], J. S. D. Blake[a], R. E. Johnson[a]

[a]*Department of Physics & Astronomy, University of Leicester, UK*
[b]*Space Environment Technologies, USA*
[c]*Department of Physics, Lancaster University, UK*
[d]*Jet Propulsion Laboratory, USA*
[e]*Department of Physics & Astronomy, University College London, UK*
[f]*Center for Space Physics, Boston University, USA*
[g]*Central Arizona College, USA*
[h]*Institut d'Astrophysique et de Géophysique, Université de Liége, Belgium*
[i]*Institut de Recherche en Astrophysique et Planétologie, Université de Toulouse, CNRS, France*
[j]*Division of Geological & Planetary Sciences, California Institute of Technology, USA*

Abstract

On 21 April 2013, during a co-ordinated Saturn auroral observing campaign, the northern and southern poles of the planet were observed from the Earth using the NASA Infrared Telescope Facility (IRTF), Keck, and Hubble Space Telescope (HST) simultaneously with the Cassini infrared, visible, and ultraviolet remote sensing instruments. We present simultaneous multi-scale and multi-wavelength analysis of the morphology of auroral emissions at Saturn. The visible main auroral emission vary between ∼2 and 10 kR on timescales of minutes and across spatial scales of down to ∼14 km on the planet. The H_2 Far Ultraviolet (FUV) brightness varies by a factor of ∼10, from ∼4-40 kR, over timescales of 1 minute and spatial scales of 720 km. H_3^+ infrared emissions vary less than the H_2 emissions, from ∼5-10 µWm^{-2}sr^{-1}, over similar spatial scales (∼300 km) and timescales of a few seconds to a few hours. The fine-scale temporal and spatial features seen in the main oval show that complex structures are present even during quiet solar wind conditions. Diffuse ultraviolet emissions southward of the southern midnight main oval that are not seen in the infrared, implying a steep temperature gradient of ∼50 K over 2-4° latitude equatorward of the main oval. Dynamics on scales of ∼100 km at the poles are revealed by lower spatial resolution observations, the morphologies of which are partly consistent with overlapping local-time fixed and co-rotating current systems. We also present the first direct comparison of simultaneous infrared, visible, and ultraviolet auroral emissions at Saturn. Finally, the main auroral emissions are found to be approximately co-located in the midnight sector, forming an arc with a width of ∼0.5-1°, at 72-74° southern latitude, moving slightly equatorward with increasing local-time.

Keywords: Saturn, Atmosphere, Magnetosphere, Aeronomy

1. Introduction

The upper atmosphere of Saturn is mostly composed of neutral atomic and molecular hydrogen. Co-located with this is the ionised part of the upper atmosphere, the ionosphere, is dominated by H^+ (protons) and H_3^+. When energetic electrons enter the upper atmosphere of a giant planet, by way of precipitation delivered along the magnetic field lines, they can either excite or ionise the constituents therein. Badman et al. (2014) reviews the auroral process in detail.

Auroral emissions at ultraviolet and visible wavelengths are a direct result of the interaction between the atmosphere and precipitating electrons. Secondary electrons resulting from this interaction excite the molecular hydrogen which produce photons in the 70-180 nm range and visible H_2 transitions from 'higher' to 'lower' Rydberg states (Shemansky and Ajello, 1983). At lower altitudes some of this emission, mainly below 135 nm, is attenuated by the hydrocarbon layer situated at or above the aurora. The amount of H_2 absorption by these hydrocarbons, measured by the color ratio CR=I(155-162 nm)/I(123-130 nm), where I is the brightness in a certain spectral range, is correlated to the penetration depth via atmospheric modelling, and hence the primary energy, of the precipitating electrons. When no absorption is observed, the CR of the emergent emission is 1.1 (Gustin et al., 2013, and references therein). H Lyman-α is produced by de-excitation from the $n = 2$ to the fundamental $n = 1$ electronic level of H atoms, while the visible Balmer series is due to the de-excitation from $n > 2$ to the $n = 2$ level of H (Aguilar et al., 2008).

When molecular hydrogen is ionized, it is rapidly converted to H_3^+ by the exothermic reaction

$$H_2^+ + H_2 \longrightarrow H_3^+ + H, \tag{1}$$

where the energy required to produce H_2^+ is delivered either via energetic particles or solar extreme ultraviolet (EUV) photons. The intensity of the infrared H_3^+ emission is both an exponential function of ionospheric temperature (Neale et al., 1996; Miller et al., 2013) and a linear function of the ionisation rate of H_2. The emission rate of a particular H_3^+ emission line is given by

$$I = N \frac{K^i}{Q(T)} \exp\left(-\frac{hc\omega_u^i}{kT}\right), \tag{2}$$

Email address: hmelin@spacewx.com (Henrik Melin)

where N is the number of H_3^+ ions that are emitting thermal emission at temperature T, k is Boltzmann's constant, ω_u^i is the wavenumber of the upper energy level of the transition i, $Q(T)$ is the temperature dependent partition function given by Miller et al. (2013), h is Planck's constant, c is the speed of light, and K^i is a composite constant determined by the properties of the transition i we are considering. For more information see e.g. McCall (2001).

The analysis of auroral emissions in each wavelength band tells us about different aspects of the precipitation process and how this injection of energy affects the makeup of the upper atmosphere. The auroral morphology tells us where in the magnetosphere the precipitation originates from, and via analysis of infrared and ultraviolet spectra one can monitor physical parameters like ion density, thermospheric temperature, precipitation flux, and precipitation energy of the auroral primaries.

The time between electron impact and emission in the UV and in the visible of H and H_2 is very short, about 10^{-2} s (Menager et al., 2010; Badman et al., 2014), giving an instantaneous view of the precipitation process. In contrast, H_3^+ radiates thermally and can have lifetimes of around 500 s (Melin et al., 2011a), producing a temporally averaged view of the auroral radiation during the lifetime of the ion. Therefore, both the integration times of the instrumentation and the chemical lifetimes of the species concerned become important factors when comparing simultaneous infrared and ultraviolet/visible auroral emissions.

For example, Melin et al. (2011a) analysed simultaneous infrared and ultraviolet observations of Saturn's southern aurora at a high spatial resolution and noted that, outside of the main oval emission, the intensity of H_3^+ did not necessarily map well to that of either H or H_2, with a diffuse equatorward oval being most prominent in H Lyman-α. These differences are likely attributable to both the fact that the intensity of emission of the H_3^+ ion is strongly dependent on temperature, and that it has a lifetime of about 500 s. In contrast, multispectral analysis of Lamy et al. (2013) observed a one-to-one correspondence between the emission seen in the infrared and ultraviolet.

One of the most intriguing features of the Saturn system is the presence of rotating phenomena near the planetary rotation period, but with two separate periods that slowly evolve with time, one associated with the northern hemisphere and the other with the southern (Galopeau and Lecacheux, 2000; Espinosa and Dougherty, 2000; Gurnett et al., 2009; Provan et al., 2009; Andrews et al., 2010; Southwood and Cowley, 2014; Provan et al., 2014). The signatures of these periodic phenomena, known as the planetary period oscillations (PPO), are present in many observations, e.g. Saturn kilometric radiation (SKR, Gurnett et al., 2009; Lamy et al., 2011), the infrared H_3^+ aurora (Badman et al., 2012b; Lamy et al., 2013; O'Donoghue et al., 2015), the ultraviolet H_2 aurora (Lamy et al., 2009; Nichols et al., 2010a; Lamy et al., 2013; Bunce et al., 2014), the magnetospheric energetic electrons (Carbary et al., 2009), and the magnetopsheric magnetic field (Southwood and Kivelson, 2007;

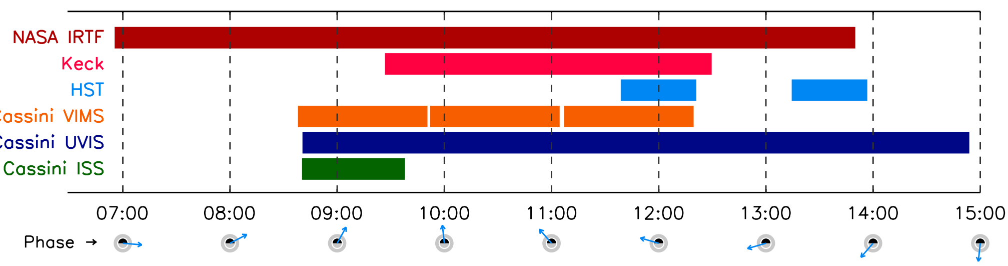

Figure 1: The UT intervals on 21 April 2013 (2013-111) during which a particular instrument was acquiring data. The arrow in the illustration of Saturn at the bottom indicates the azimuth of the effective southern PPO dipole direction ($\Phi_S = 85°$ at 07:00 UT, as measured duskward from noon). The arrow shows the rotation of the planet as seen from above the northern pole, with the Sun towards the bottom. Note that 10:00 UT corresponds to midnight in Hawaii Standard Time, the time-zone of the IRTF and Keck telescopes. The first three instruments observed the northern dayside, whilst the last three observed the southern midnight sector.

Instrument	Start Time	End Time	Exposures
NASA IRTF CSHELL	06:55	13:50	75 × 120 s
Keck NIRSPEC	09:26	12:29	57 × 60 s
HST ACS Orbit 1	11:38	12:12	2 groups of 5 × 100 s
HST ACS Orbit 2	13:14	13:47	2 groups of 5 × 100 s
Cassini VIMS	08:38	12:19	3 groups of 64 × 64 × 1 s
Cassini UVIS	08:40	14:53	373 × 60 s
Cassini ISS	08:40	09:41	37 × 180 s

Table 1: The simultaneous remote sensing observations of Saturn analysed in this study for day 111 of 2013. This is presented as a time-line in Figure 1. The times of the IRTF, Keck, and HST observations are adjusted to be equivalent to UT at time of emission from the planet's 'surface'.

Provan et al., 2009; Andrews et al., 2012). Badman et al. (2012b) observed the intensity of the auroral H_3^+ emission in each hemisphere to be dependent on both local-time and the appropriate PPO phase. This is consistent with the superposition of two current systems, one fixed in the Sun-Saturn frame, the other rotating at the PPO period. The ultimate origin of the rotating current systems has been proposed to be driven by either the magnetosphere (Goldreich and Farmer, 2007) or the atmosphere (Smith, 2006; Jia et al., 2012; Southwood and Cowley, 2014). In the latter case, it remains an open question as to what mechanism could provide the required relatively stable and sustained atmospheric vortices (Smith, 2014).

The main auroral oval of Saturn maps near to the boundary between open and closed field-lines (Cowley et al., 2004; Bunce et al., 2008; Carbary et al., 2008; Belenkaya et al., 2011). On or close to this oval there are a number of specific features that are attributed to separate processes. These include dawn brightened signatures of Dungey cycle plasma convection (Cowley et al., 2005), interactions between Saturn's magnetosphere and the solar wind at the magnetopause (Gérard et al., 2005; Radioti et al., 2011; Badman et al., 2013; Meredith et al., 2014), and signatures of injections from the hot plasma populations in the night-side magnetosphere (Mitchell et al., 2009b; Grodent et al., 2010; Lamy et al., 2013).

Saturn's ultraviolet emissions were first discovered by a rocket-borne spectrograph in 1975 (Weiser et al., 1977), whereas H_3^+ was first detected by Geballe et al. (1993) using the United Kingdom Infrared Telescope (UKIRT). It was not until the arrival of the Cassini spacecraft that visible auroral emissions were discovered (Kurth et al., 2009). The infrared, visible, and ultraviolet auroral emissions have been used in multiple studies as a diagnostic for the ionosphere–magnetosphere–thermosphere interaction but also as an in-situ diagnostic of the physical conditions in the thermosphere. See Bhardwaj and Gladstone (2000), Kurth et al. (2009), and Badman et al. (2014) for excellent overviews.

Lamy et al. (2013) analysed a set of radio, infrared, ultraviolet, and energetic neutral atom (ENA) Cassini observations over the duration of a full Saturn rotation. This set of observations coincided with an injection event in the magnetotail, producing dawn intensifications of the auroral oval seen in both the infrared and ultraviolet remote sensing data. They also noted features in the auroral emissions compatible with two superimposed current systems, one fixed in local-time and one rotating at the PPO phase, as outlined above.

Most remote sensing studies of Saturn's aurora have used observations from a single vantage point, obtained from either the surface of the Earth, low altitude Earth orbit, or from the Cassini spacecraft in orbit at Saturn. By definition, such observations cannot get a complete view of the northern and southern auroral ovals, since at least one portion of the system is hidden from view. Ground-based observations are limited by always observing the sunlit hemisphere, such that the effects of solar-related emissions cannot easily be disentangled from those created by auroral processes. A study of Cassini-UVIS, FUSE (Far Ultraviolet Spectroscopic Explorer), and HST-STIS (Space Telescope Imaging Spectrograph) auroral spectra showed that the energy of the primary electrons responsible for the UV aurora are 20 keV or lower (Gustin et al., 2009). The most energetic electrons would produce a peak auroral emission altitude of just 640 km (Gérard et al., 2013), lower than the 900 to 1300 km derived from HST images (Gérard et al., 2009) and the 1100 km derived from infrared Cassini observations (Stallard et al., 2012).

Here, we compare the morphology of simultaneous remote sensing auroral observations from the 2013 Saturn auroral observing campaign on both the dayside and nightside of the planet. This is achieved by combining observations using ground-based infrared telescopes, the Hubble Space Telescope, and infrared, visible, and ultraviolet remote sensing instruments onboard the Cassini spacecraft.

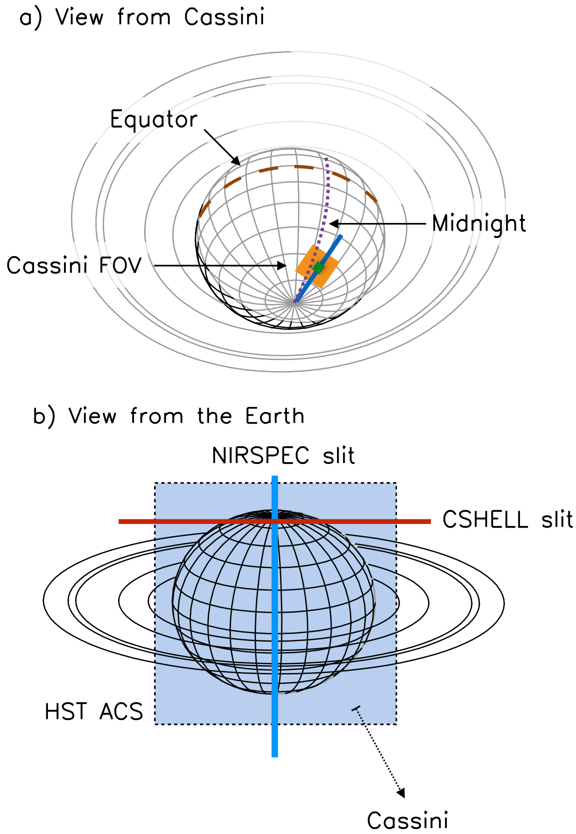

Figure 2: Saturn as seen from a) the Cassini spacecraft and b) the Earth on 21 April 2013 (2013-111) at 10:00 UT. Cassini is viewing the nightside, whereas the Earth-based observatories view the sunlit hemisphere. During this interval the equatorial angular diameter of Saturn was 18.8″ as seen from the Earth and 12.8° as seen from Cassini. Indicated in a) is the field-of-view (FOV) of the Cassini remote sensing instruments; also shown in greater detail in Figure 3. Panel b) shows the FOV of the Keck NIRSPEC slit (2.09 µrad or 0.432″ wide), the NASA IRTF CSHELL slit (2.42 µrad or 0.5″ wide), and the HST ACS (covering 35 × 31″ or 170 × 150 µrad). The dotted arrow shows the direction of Cassini.

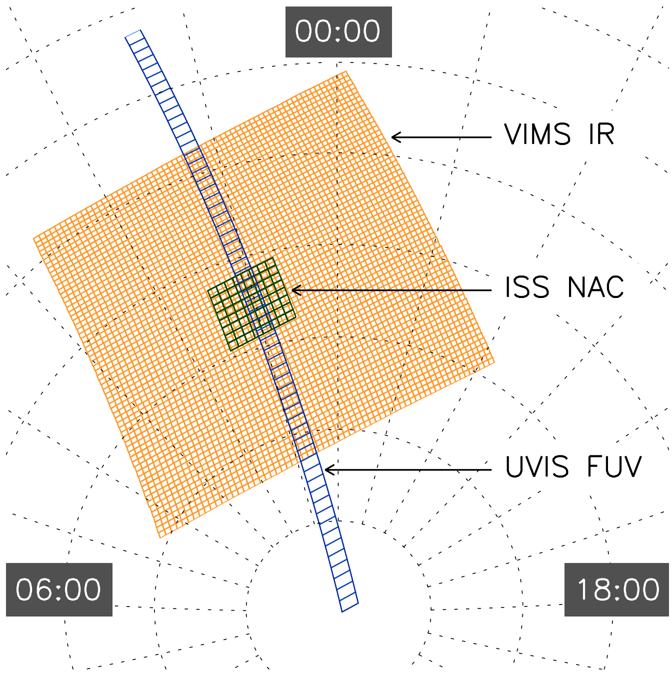

Figure 3: The latitude and local-time projection of the Cassini VIMS infrared channel, the ISS Narrow Angle Camera (NAC), and the UVIS Far Ultraviolet (FUV) channel FOVs as seen at 10:00 UT 2013-111, covering the midnight sector of the southern pole of Saturn. The view is through the planet from the north pole. For both VIMS and UVIS, each pixel is shown, whereas for ISS, each square contains 128 × 128 actual pixels. The grid has a spacing of 5° in latitude and 1 h in local-time. The spatial resolutions of these three remote sensing instruments are very different indeed, with the mean resolutions on the planet being 720, 280, and 14 km/pixel for UVIS, VIMS, and ISS, respectively.

2. Observations

The coordinated Saturn auroral observing campaign took place in April and May 2013, and involved the use of Cassini (remote sensing and in-situ instruments), the HST, the NASA Infrared Telescope Facility (IRTF), the W.M. Keck II (hereafter Keck), and the Very Large Telescope (VLT). During these two months there were a variety of temporal overlaps between observations using these instruments, but 21 April 2013 (2013 day-of-year 111, hereafter 2013-111) stands out as particularly interesting. On this day all but one (VLT) of the facilities acquired data, and during an 8-hour period at least one of the six remaining instruments were observing, with as many as five taking data simultaneously. Each instrument involved in this campaign has unique capabilities, revealing different aspects of the auroral process.

During 2013-111, the Earth-based platforms (IRTF, Keck, and HST) were observing the dayside of Saturn at the same time as Cassini was observing the nightside, providing an opportunity to measure simultaneous dayside and nightside auroral emissions in multiple wavelength bands. The timeline of the observations can be seen in Figure 1, with the geometry being shown in Figures 2 and 3.

Table 1 details the observations analysed in this study and Table 2 summarises the capabilities of each instrument. Granular details on how the instruments operate and the data reduction can be seen in Appendix A. It is important to note that none of these instruments offer the same capability, with each having slightly different operational modes and angular resolutions. As we shall see, this creates both opportunities and hurdles for the comparative science that can be achieved.

In figures detailing the observations, where it is appropriate, the azimuth of the northern and southern PPO phase, Φ_N and Φ_S respectively, are shown as arrows in a view looking down onto the north pole with noon at the bottom. These vectors show the direction of the quasi-uniform equatorial perturbation magnetic fields associated with the PPOs at these times, as well as the direction of the effective transverse dipole associated with the corresponding polar field perturbation (e.g. Andrews et al., 2010; Lamy et al., 2011). These rotate at the corresponding PPO period in the same sense as planetary rotation. The specific phases employed here were derived from concurrent Cassini magnetic field data by Provan et al. (2014). During 2013-111 the rotation periods are 10.641 h for the northern system and 10.694 h for the southern. The maximum upward field-aligned currents (FACs) associated with these rotating magnetic fields are expected to be located at $\Phi_S + 90°$ in the south and $\Phi_N - 90°$ in the north (Andrews et al., 2010) - these positions are shown as lines. We define the PPO longitude, $\Psi_{N,S}$, to be $\Psi_{N,S} = \Phi_{N,S}(t) - \phi$, where ϕ is the azimuth angle from the PPO phase, $\Phi_{N,S}$, increasing in the direction of planetary rotation, as per Hunt et al. (2014).

Since auroral emission is expected to be driven by the upward FACs (e.g. Bunce et al., 2008), the FACs associated with the PPO system are also locations of enhanced auroral brightness (Badman et al., 2012b; Nichols et al., 2010a). A comparison between the expected enhancement in brightness, governed by the phase of $\Phi_{N,S}$, and the observed auroral brightness, as seen in both the infrared and the ultraviolet, is explored in Section 3.3.

In the following sections we describe the morphology of the auroral emission as observed through each instrument's FOV. Table 3 summarizes the key findings of each observation.

2.1. Cassini VIMS

Figure 4 shows the latitude and local-time projected VIMS observations of auroral H_3^+ emission, with the grid having a spacing of 1 h in local-time and 5° in latitude. During this interval, the mean spatial resolution of a VIMS pixel on the planet is 280 km/pixel, providing a detailed view of the southern midnight auroral oval, covering about 6 hours of local-time, and centered about one hour post-midnight (1 am). The dashed line indicates Φ_S PPO phase, with the illustrations of Saturn

Instrument	Wavelength	FOV (spatial pixels)	t_{exp}	Notes
Cassini VIMS	IR, 0.8 - 5.2 μm	32 × 32 mrad (64 × 64)	1 s pixel^{-1}	Integrates one pixel at a time. Has 256 spectral elements.
Cassini UVIS	UV, 90 - 190 nm	1.5 × 64 mrad (1 × 64)	60 s	Has 1024 spectral elements.
Cassini ISS	VIS, 0.2 - 1.1 μm	6.1 × 6.1 mad (1024 × 1024)	3 min	Using the clear filter.
HST ACS	UV, ∼130 nm	170 × 150 μ μrad (1024 × 1024)	8 min	Using the F125LP filter.
IRTF CSHELL	IR, ∼4.0 μm	2.4 × 145 μrad (2.5 × 150)	∼40 min	Has 256 spectral elements.
Keck NIRSPEC	IR, 3.9 - 4.1 μm	2.2 × 116 μrad (3 × 167)	1 min	Has 1024 spectral elements.

Table 2: Summary of the basic characteristics of the remote sensing instruments used in this study, with wavelengths given in the infrared (IR), visible (VIS), and ultraviolet (UV). The angular field of view (FOV) is given in the second column, with the number of pixels that this area subtends given within brackets. The total exposure time required to produce the figures presented in this paper are given by t_{exp}, and are governed principally by signal-to-noise (S/N). All the instruments are described in greater detail in Appendix A.

Instrument	Fig.	§	Hemisphere	Key features
Cassini VIMS	4	2.1	S	1. Thin main auroral oval, with no other auroral emission present 2. Distinct discontinuity present at about $\Psi_S = 0$
Cassini UVIS	5	2.2	S	1. Main oval, varying in intensity and location at a constant local-time 2. Diffuse equatorward emission between -68 and -70° latitude
Cassini ISS	6	2.3	S	1. Fine structure within the main oval 2. High degree of spatial and temporal variability
HST ACS	7	2.4	N	1. Thin main auroral oval indicating quiet auroral conditions 2. Diffuse equatorward oval seen in UVIS data is not present
IRTF CSHELL	8	2.5	N	1. Low signal-to-noise and guiding problems 2. Northern oval varies over timescales of hours
Keck NIRSPEC	9	2.6	N, S	1. Total northern intensity intensifies over time. 2. Northern noon main oval fades away over time. 3. Southern noon oval becomes brighter over the same interval

Table 3: Summary of the key features seen in each instrument during the interval in 2013-111 considered here, described in more detail in Section 2. References to figures and sections (§) are listed in the table, along with which hemisphere is observed, north (N) and/or south (S).

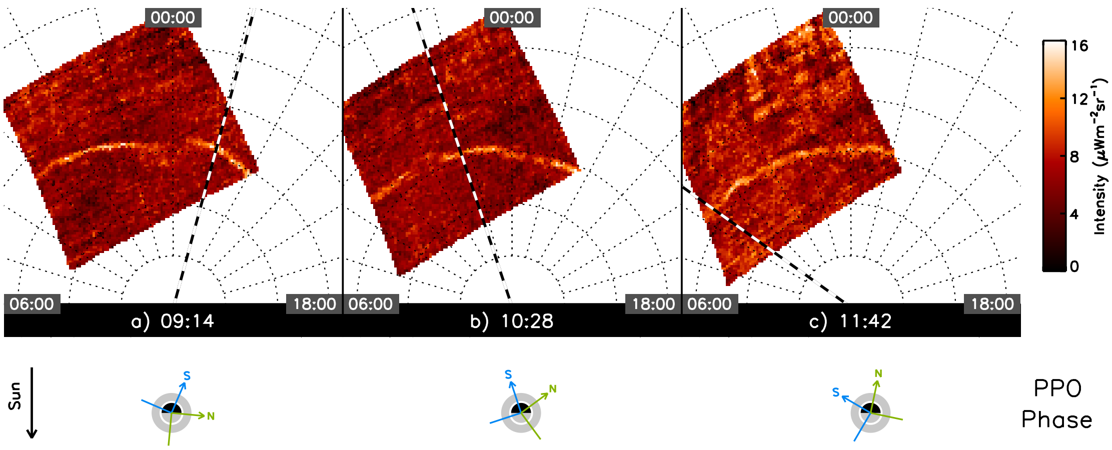

Figure 4: Latitude and local-time projection of the auroral H_3^+ emissions observed by Cassini VIMS at the southern pole of Saturn on 2013-111. Dawn is towards the left, midnight towards the top, and dusk towards the right, i.e. the view is through the north pole onto the south pole of the planet. The grid spacing is 1 h in local-time and 5 degrees in latitude. The illustrations of Saturn at the bottom show the planet as viewed from above the north pole, with the sun towards the bottom. The arrows indicate the azimuth of the PPO phase, where N and S indicate Φ_N and Φ_S respectively. Lines orthogonal to the arrows are the expected locations of the peak upward FACs, i.e. $\Phi_N - 90°$ for the north and $\Phi_S + 90°$ for the south. The dashed line in the projections show Φ_S.

beneath the images showing both the northern and southern PPO phase, together with the location of the expected peak of the upward FAC. The auroral emission is confined to a thin band located between -72° and -75° latitude, consistent with the mean auroral location of -74° of Badman et al. (2011). There is a discontinuity at about midnight in Figure 4a, which rotates into the morning sector, appearing approximately fixed in PPO longitude. There is also a kink apparent at midnight in Figure 4b, which is seen rotated in Figure 4c. Most of these H_3^+ emission features appear fixed in PPO longitude. For example, the discontinuity remains ahead of Φ_S by approximately the same amount in both Figures 4a and 4b.

2.2. Cassini UVIS

Figure 5 shows the brightness of a) H_2 Lyman and Werner bands and b) H Lyman-α as observed by UVIS, projected to latitude and time of exposure (given in UT), between 08:00 and 15:00 UT. The two color-bars show the brightness and the calculated electron energy flux. To convert the H_2 brightness to precipitating power, we assumed that 10 kR emissions are produced by an electron energy flux of 1 mWm^{-2} (Gustin et al., 2012, and ref. therein). The southern PPO longitude beneath the center of the UVIS slit, Ψ_S, is shown on the top y axis. Because the Cassini pointing was approximately fixed at $\sim$ 01:00 LT, as shown in Figure 3, the

UVIS emissions in Figure 5 show how the brightness changes along the spectrograph slit as the planet rotates underneath it. However, the infrared VIMS observation provides a 2D view of the morphology, indicating that the emission is approximately fixed with rotation. Both VIMS and UVIS see the discontinuity and the poleward motion of the main oval, with UVIS seeing a subsequent equatorward movement after 11:00 UT, after which there are no more VIMS images.

Figures 5a and b show main oval emission at about -74°, consistent with the dayside statistical location of the UV oval of Badman et al. (2006). There is also weaker and diffuse equatorward emission between about -70° and -68° latitude. The auroral intensity weakens significantly at 10 UT, consistent with the discontinuity seen by VIMS rotating under the UVIS slit. There is bright emission in both H and H_2 at 09:00 and at 11:00 UT. After this time the main oval dims and brightens slightly at about 13:30 UT.

After 10:00 UT there is a poleward motion of the poleward main auroral emission, whilst the equatorward emission moves further towards the equator. At about 13:00 UT these two auroral bands have returned to their original position.

2.3. Cassini ISS

The ISS camera covers a visible wavelength range of 0.2 to 1.1 µm, which includes H Balmer-α and H_2 emissions. These observations offer a very narrow field of view of the auroral emission near the southern pole, covering only a few degrees of latitude, as shown in Figure 3. The latitude and local-time projected ISS observations are shown in Figure 6, with the dashed line showing lines of constant PPO longitude, indicating the rotation of the planet. There is a clear arc of emission rotating into the dawn sector, approximately fixed relative to the rotation of the planet. The ISS images have a background level of counts produced by thermal noise in the instrument, which adds a near constant brightness of $\sim$5 kR, which is a similar level to that of the main oval itself, which has been subtracted off.

Figure 6 shows structure within the main oval, with bright spots and dark bands appearing and disappearing between exposures, in particular Figures 6c, j, and k. These features are as small as a few tens of km. There is significant short-term variability in brightness, with Figure 6j showing a bright spot on the main oval that dims over timescales of minutes. As indicated by the arrows, there is evolving filamentary structures in Figures 6g and 6h, which also show highly variable behavior, both spatial and temporal.

2.4. HST ACS

Shown in Figure 7 are the four HST images obtained during the interval considered here, projected to a latitude and local-time grid. On the small illustrations of Saturn below the HST images, the northern and southern PPO phases are shown, in addition to the location of the peak FAC as in the previous diagrams. The viewing geometry is shown in Figure 2b.

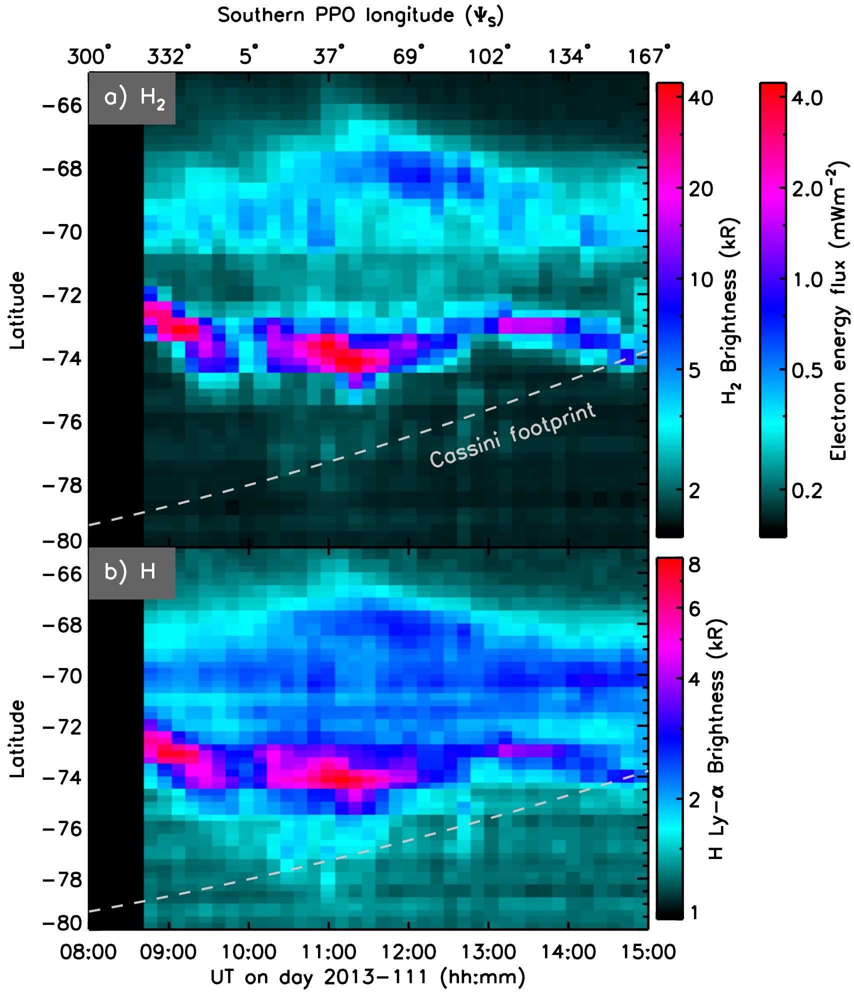

Figure 5: UVIS data showing brightness of a) H_2 Lyman and Werner bands and b) H Lyman-α emissions projected to latitude and UT, between 08:00 and 15:00 on 2013-111. These observations are approximately fixed in local-time, ∼01:00 UT, as illustrated in Figure 3. The top right scale shows the calculated electron energy flux required to produce the observed H_2 brightness (Gustin et al., 2012). The top x axis shows the Ψ_S PPO longitude under the center of the UVIS slit. An upward FAC associated with the PPO system producing enhanced emission is predicted to occur around $\Psi_S \simeq 270°$ whilst downward current and suppression of emission occur at $\Psi_S \simeq 90°$. The equator is towards the top, and the pole towards the bottom. The main emissions are located between -72° and -74° latitude, with significant equatorward emission being present between -68° and -70°.

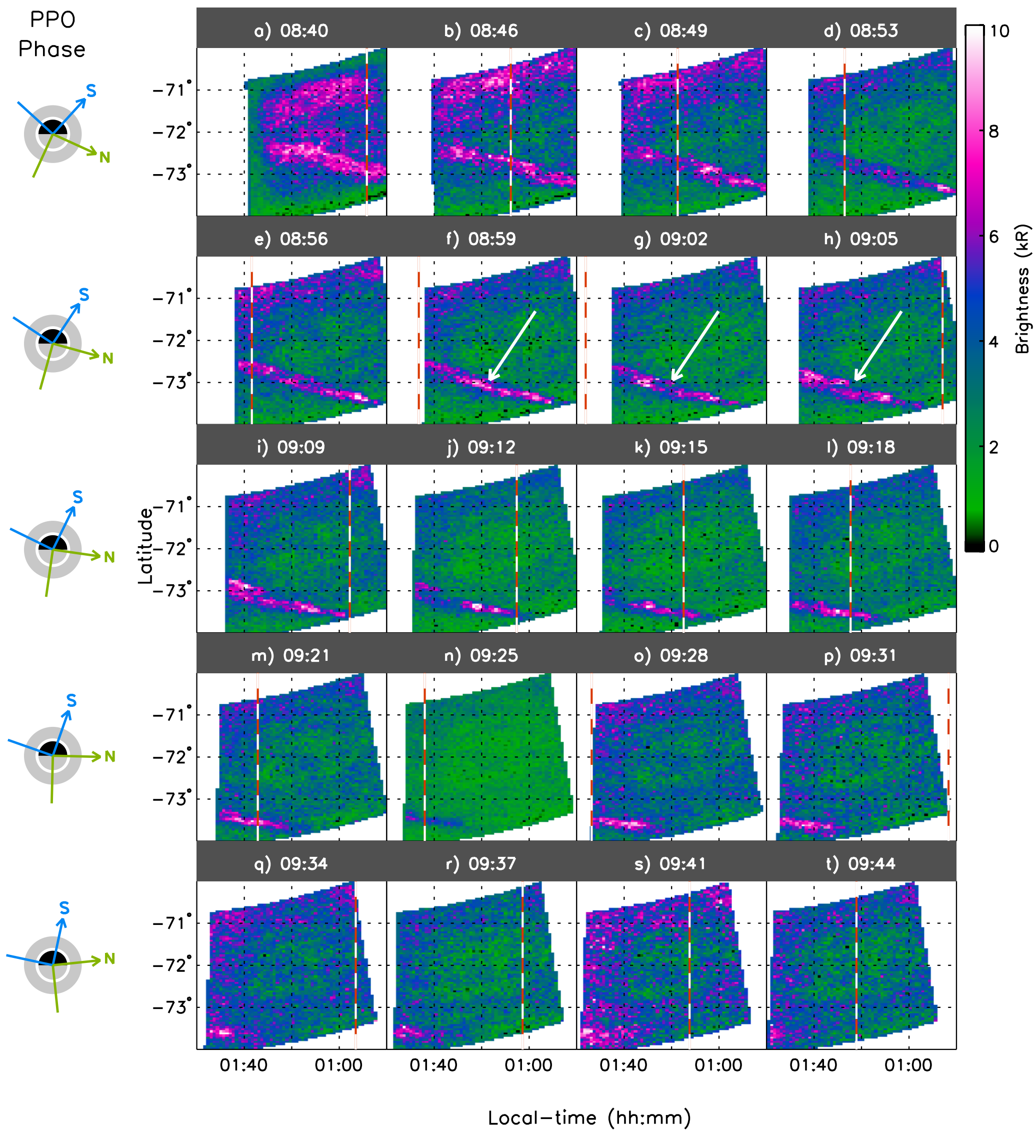

Figure 6: The latitude and local-time projected ISS observations of auroral H Balmer-α and H_2 emissions near the southern pole of Saturn on day 2013-111. The grid spacing is 1° in latitude, equivalent to ∼1000 km on the planet, and 20 minutes in local-time. Subfigures a) through t) show the first 20 images in a sequence of 37, with these being the only ones that show clear evidence of auroral emission. The dashed lines indicate meridians of constant PPO longitude (arbitrary), showing the rotation of the planet. The fact that the projected ISS frames migrate slowly towards dawn indicates that the pointing of Cassini is slowly drifting towards later local-times. The schematics of Saturn on the left show the PPO phase for the leftmost of the ISS observations (see Figure 4 for a description of the layout). The white arrows indicate examples of small-scale, filamentary structures as described in the text.

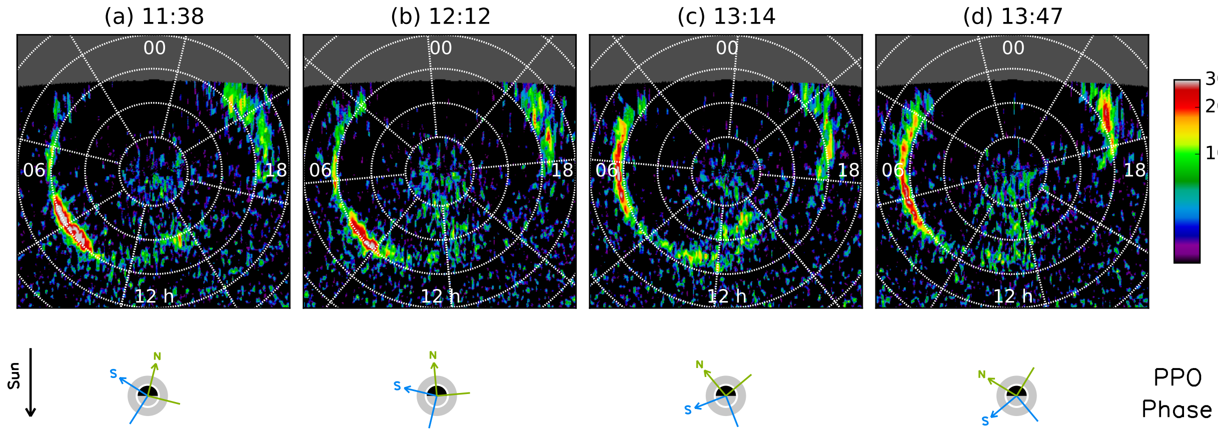

Figure 7: The HST ACS observations of Saturn's northern pole on 2013-111 projected to latitude and local-time, showing emission in the F125LP filter containing H_2 Lyman and Werner band emissions. The grid spacing is 5° in latitude and 3 h local-time (arbitrary). The schematics of Saturn show the PPO phases during these observations, as in Figure 4. The values for Φ_N are a) 166°, b) 185°, c) 220°, and d) 329°. Note that the midnight sector is not observable by the HST, here shaded grey.

The images in Figure 7 show relatively quiet auroras. They are similar to those observed by Cowley et al. (2004) and Gérard et al. (2006) during quiet magnetospheric conditions, and very much unlike those observed by Nichols et al. (2014) on 2013-95 and 2013-140, which were active. There is a dawn-side enhancement in all four images. The last image shows a brightening of the dusk side oval. All images in Figure 7 show diffuse emission poleward of the main auroral oval at local noon – most clearly shown in c), appearing static in local-time. Note that the midnight sector is not visible with this viewing geometry.

The total emitted UV power has been estimated for each image by converting the observed brightness in the F125LP filter to the emitted power of unabsorbed H_2 auroral emission in 700-1800 Å, as given in Table 2 of Gustin et al. (2012), assuming a CR of 1.1, which is the unabsorbed value. This conversion is obtained by applying hydrocarbon absorption and total HST throughput to an unabsorbed H_2 spectrum to obtain a simulated observed spectrum. The total emitted power is then calculated assuming a mean H_2 photon energy of 10 eV and a HST-Saturn distance of 1.32×10^9 km. The total powers for the four images in Figure 7 are 28, 28, 28, and 27 (± 1) GW, respectively. Despite the variable morphological nature of the emissions present in the individual HST images in Figure 7, there is very little actual change in total power output.

2.5. NASA IRTF CSHELL

Figure 8 shows 8 spectral images of ∼40 minutes integration time, and then a summed total; the spatial dimension is along x (horizontal) and spectral dimension is along y (vertical). The spectral dimension covers 1.65 nm, and is centered at 3.953 µm. This displays the H_3^+ Q(1, 0^-) intensity across Saturn's northern polar cap, with the dawn region towards the left, eastward on the sky. The motions of the ions, as they flow towards the observer at dawn and away at dusk, produce a wavelength Doppler shift that can be measured using CSHELL. This can be seen as a slight negative slope in the summed H_3^+ Q(1, 0^-) emission line in Figure 8i.

Whilst the signal-to-noise is low in Figure 8, there is clear variability over the entire interval from 07:14 to 13:14 UT. This interval starts with the auroral H_3^+ emission being weak, barely visible over the noise floor of the observations. After almost disappearing at 09:18 UT, it brightens considerably between 10:09 UT and 12:14 UT, initially noon-brightened, then appearing dusk-brightened at 11:18 UT. After 12:14 UT, the emission dims significantly, and is not readily seen at all at 13:14 UT. The summed intensity over this interval, seen in Figure 8i, is relatively evenly distributed across the polar cap.

As described in Appendix A.3, there were significant telescope guiding problems during this interval, imposing large uncertainties on both the intensity and the derived ion velocities.

2.6. Keck NIRSPEC

Figure 9 shows the intensity of the Q(1, 0^-) H_3^+ spectral line at 3.953 µm across the entire Keck NIRSPEC slit, traversing both the midnight and noon parts of the northern oval, followed by reflected sunlight from the rings, and finally, at the bottom, is the noon part of the southern auroral oval. In this wavelength range, the brightest emission by far is the ring sunlight reflection, and it has been capped in a manner that most clearly shows the H_3^+ emission at the poles. The northern noon part of the oval is only seen between 09:30 and 10:30 UT, and appears to undergo a poleward contraction between 10:00 and ∼10:30 UT. The southern noon oval is weak at the beginning of this interval, intensifying near 12:00 UT. The intensities of both the southern and northern main ovals vary significantly over the ∼3 hours of observations analysed here, up to 50% of the mean. The H_3^+ emissions do not display any obvious north–south conjugate behavior in intensity, apart from the dimming that occurs at about 11:00 UT.

The pole-to-pole H_3^+ emission in Figure 9 shows structures in intensity at northern low- to mid-latitudes, some of which are persistent over ∼30 minutes. These emissions have been reported by O'Donoghue et al. (2013) as being produced by the inflow of material from the rings along magnetic field lines that alter the chemical makeup of Saturn's upper atmosphere (Connerney and Waite, 1984; Prangé et al., 2006). The variable but relatively long-lived horizontal low-latitude structures seen in Figure 9 warrant further investigation, but fall outside the scope of this study.

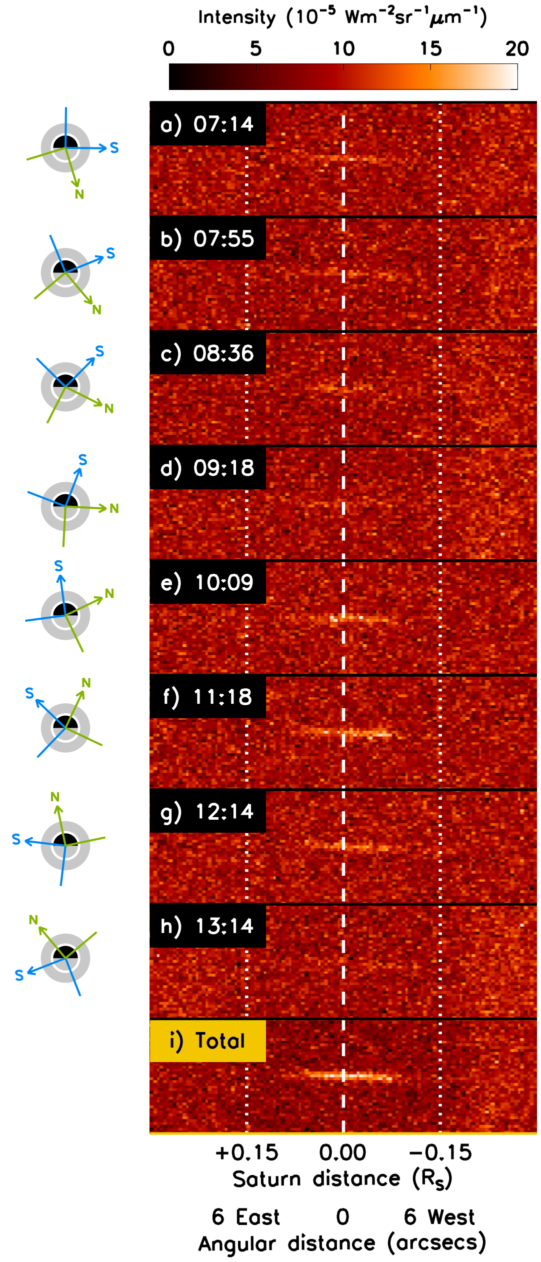

Figure 8: NASA IRTF CSHELL spectral images of the H_3^+ Q(1, 0$^-$) line at 3.953 µm, showing the intensity of Saturn's auroral emission east-west across the polar cap, as indicated in Figure 2b. The times are the half-point times of the co-added observations. The horizontal direction is spatial, while the vertical dimension is spectral, covering 1.65 nm width. Westerly angular offsets are toward dusk, with the dashed line indicating the noon meridian of the planet. The dotted lines are separated by an angular distance of 0.15 R_S (i.e. 6″) from local noon. The total profile in i) is the sum of the images a) to h) and is not on the intensity scale indicated.

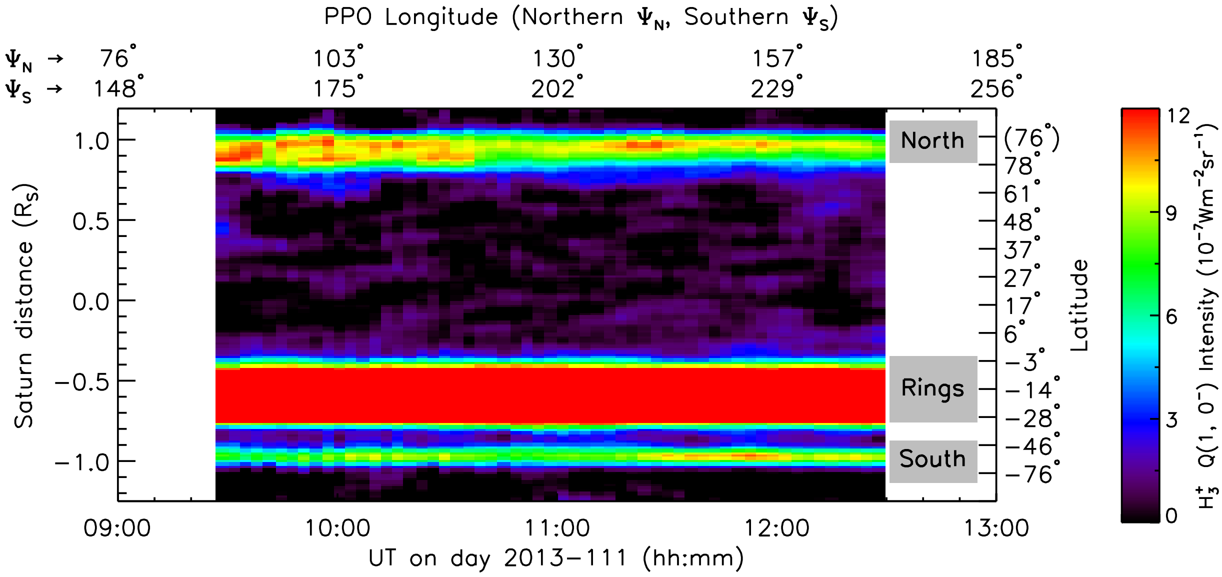

Figure 9: The infrared intensity over a narrow wavelength band centered on the Q(1, 0^-) H_3^+ spectral line along the Keck NIRSPEC slit as a function of time on day 2013-111. The slit is aligned north-south at local noon, as per Figure 2. The y-axis shows the angular distance from the center of the planet in Saturn radii (R_S) on the left and the corresponding latitude on the right, with the northern aurora, southern aurora, and the solar reflection of the rings indicated. Note that the emission seen at the rings is reflected sunlight and not H_3^+. The sub-Earth latitude of Saturn at the time of these observations was 18.2°, and the latitude in parentheses denotes that this is on the far-side of the planet.

3. Results & Discussion

The individual remote sensing observations described in the previous Section, seen in Figures 4 to 9, show emissions observed from different platforms, at different spatial scales, and in different wavelength bands. Each of these tell us something different about the auroral phenomena, and by comparing these observations we can gain a more complete picture of these processes. Below, these observations are discussed from a simultaneous multi-scale and multi-platform perspective.

3.1. Multi-Scale Behavior of the Main Aurora Oval

As we have described a set of Cassini infrared, visible, and ultraviolet observations obtained at the same time, we can compare simultaneous and spatially overlapping auroral emissions at the southern pole of Saturn in the three wavelength bands. The spatial resolution of each observation is governed by the FOV of the respective instrument, from the very high resolution ISS observations (14 km/pixel) to the lower resolution UVIS observations (720 km/pixel). Figure 10 shows these

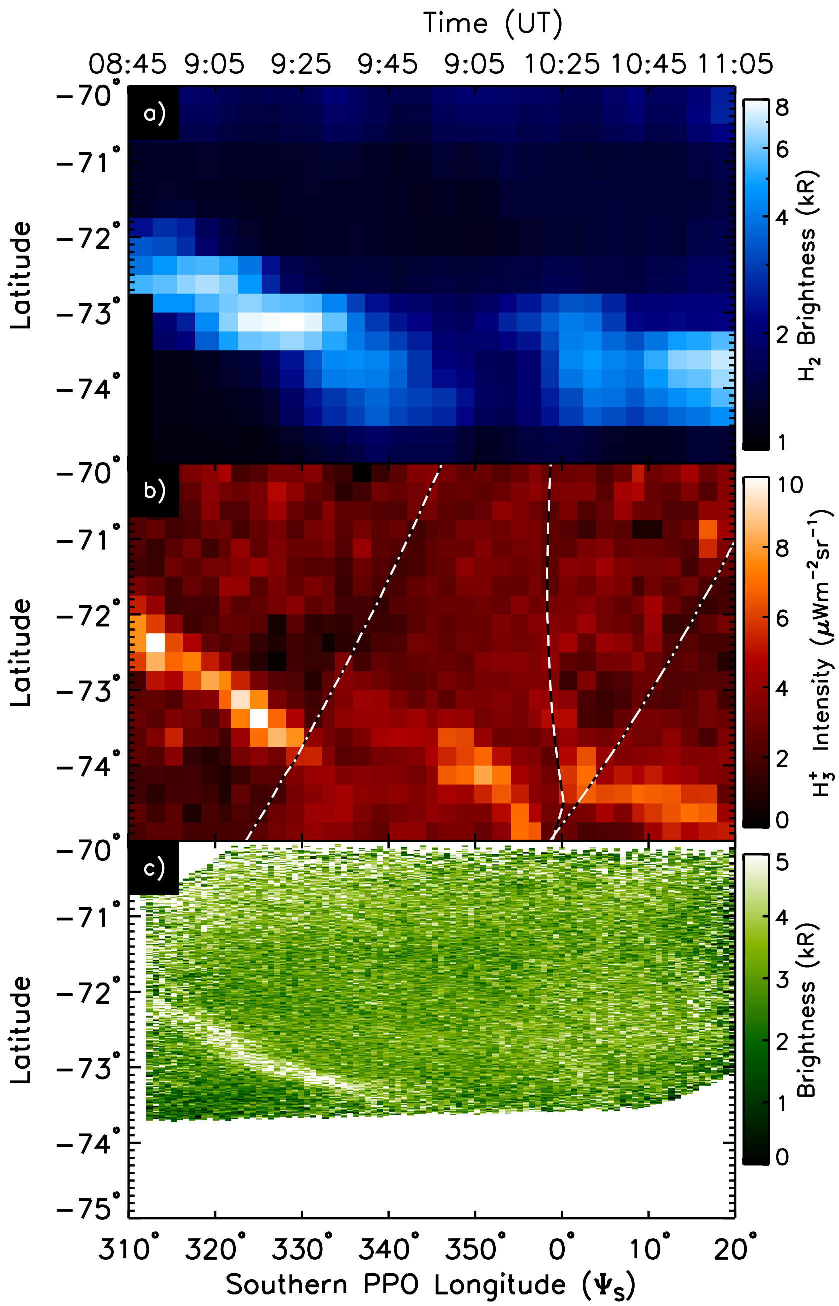

Figure 10: The a) ultraviolet UVIS H_2 bands, b) infrared VIMS H_3^+ and c) visible ISS H_2 and H Balmer-α observations obtained on 2013-111 projected to latitude and PPO longitude. In b) the outline of each VIMS exposure is shown: 09:14 UT (dashed), 10:28 UT (dot-dashed), and 11:42 UT (dot-dot-dot-dashed). The UVIS and VIMS observations can be seen plotted over a longer latitude and longitude range in Figure 12.

emissions projected to planetocentric latitude and southern PPO longitude. The figure covers 70° of rotation, focusing in on the short interval during which there are ISS observations. Both VIMS and ISS produce a sequence of images that are spatially overlapping, and in such instances the projection routine averages the emissions from all the images that occupy a particular latitude–PPO longitude location. The effect of this averaging is most clearly seen in the ISS data in Figure 10c, where the projection process produces a smooth auroral arc, seen between $\Psi_S = 310°$ and 340°, with few of the short-term temporal features seen in Figure 6. This tells us that over timescales of greater than an hour, the temporal variability seen in a set of individual ISS frames averages out to a smooth main auroral oval. Figure 10b combines three VIMS images, and the edges of each are marked as dashed, dot-dashed and dot-dot-dot-dashed lines (see Figure 12 for a broader view). There are abrupt discontinuities at these edges, particularly at PPO longitude $\Psi_S = 0°$, indicating that there is some variability in the morphology as a function of longitude or time, or both.

In Figure 10, the full-width-half-maximum (FWHM, or θ) at $\Psi_S = 325°$ of the auroral arc in the ultraviolet: $\theta_{UV} = 0.9°$, infrared: $\theta_{IR} = 0.8°$, and visible: $\theta_{VIS} = 0.5°$. The widths of the ultraviolet and infrared arcs are very similar, whilst the visible arc is considerably more narrow. This is likely related to the fact that ISS is only sensitive to the brightest of the auroral emissions, thus producing a more confined arc of emission.

Since both ISS and UVIS observe emissions produced by the same excitation mechanism, the morphology observed by the two instruments is expected to be identical. The emissions seen by both of these instruments are produced by direct excitation of atomic and molecular hydrogen by the precipitation process, making a direct comparison possible. However, since they operate at very different spatial (and temporal) scales, they capture different aspects of the auroral process: UVIS sees large-scale morphology, whilst ISS captures very fine-scale features of the emission.

Figure 11 shows the UVIS H_2 and ISS observations projected between -72° and -74° latitude and between 8:45 UT and 10:00 UT, during which ISS was acquiring data. The UVIS data in a) and the ISS data in c) are projected to 0.5° latitude and 15 minutes UT, whereas the ISS data in b) is projected to 0.01° and 30 seconds UT, with the dashed vertical lines indicating the edge of each ISS sub-image that spatially overlaps with the UVIS slit. A length scale of 1,000 km on the planet is indicated in each panel. There is variability in the main oval as observed by ISS of $\sim$5 kR inside the main oval, with spatial features being as small as a few tens of km. In addition, the width of the main oval is initially $\sim$1° but shrinks to about $\sim$0.5° after 1 hour UT. Since the fine-scale variability seen with ISS is expected to have a one-to-one correspondence with the variability present in the field-aligned currents, the high-resolution ISS observations reveal auroral processes that are not visible to the lower-resolution UVIS and VIMS instruments.

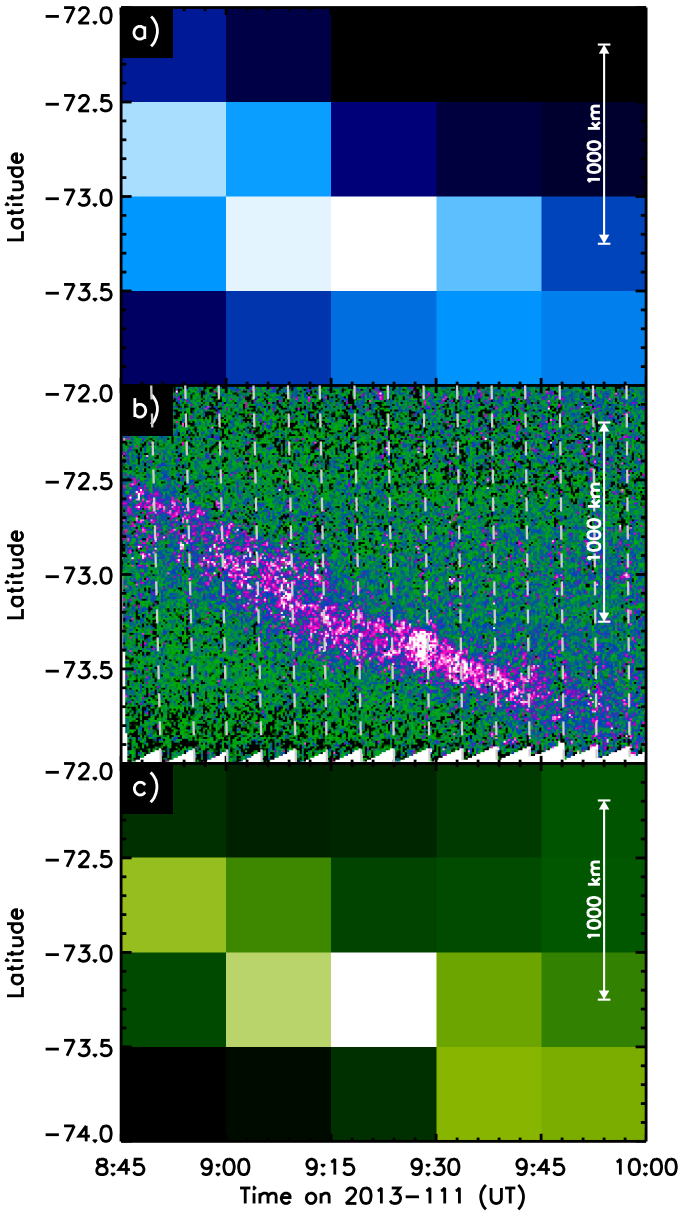

Figure 11: The a) ultraviolet H_2 UVIS, b) visible ISS, and c) ISS emission downgraded to the spatial resolution of UVIS, projected to latitude and UT time. The grid resolution for a) and c) is 0.5° and 15 minutes, and for c) it is 0.01° and 30 seconds. The individual ISS images in b) are separated by dashed lines, and only the portion of their FOV that is spatially overlapping with UVIS is shown. Whilst UVIS and ISS have very different spatial resolutions, they capture the same excitation process.

The magnetospheric conditions during this interval can be estimated by the structure of the HST emissions seen in Figure 7. They show an aurora that is narrow and stable in radius, indicating that during this interval the solar wind conditions were quiet (Crary et al., 2005; Gérard et al., 2006; Clarke et al., 2009). During intervals of active aurora, fine structures within or adjacent to the main oval have been observed (Badman et al., 2012a; Lamy et al., 2013; Nichols et al., 2014), albeit at much lower spatial resolutions. Here, Figure 11b shows that even during quiet solar wind conditions, when the main oval appears thin and relatively unchanging, there are highly variable structures inside the main oval itself. Given these results, we expect Cassini's in-situ observations of the upward FACs to be variable in current amplitude over similarly small distances, with fine structures expected to have a separation of a fraction of a degree on the planet. Provided that in-situ instruments have sufficient cadence, these small-scale structures may be visible in the FAC signatures (e.g. Talboys et al., 2009).

Figure 11c shows the ISS data downgraded to the same resolution as the UVIS projection, clearly showing a very similar morphology to the UVIS H_2 data in Figure 11a. The ISS data is much less similar to the UVIS H Lyman-α morphology (not shown), strongly indicating that the ISS auroral observations are dominated by H_2 emissions, with H Balmer-α forming a relatively minor emissive component.

The set of multi-scale Cassini observations analysed in this study shows that Saturn's aurora displays significant variability on all timescales, from minutes to hours, and on all spatial scales, from tens of km to several thousands of km, even during quiet solar wind conditions. Therefore, as is the case with Earth's aurora (Uritsky et al., 2010; Klimas et al., 2010), at Saturn we are also likely to find spatial and temporal variability on as small a spatial scale as we can observe. The fact that variability is also observed over long timescales, shows that the short-term variability is not merely stochastic, but forms part of an intricate and evolving system.

3.2. Multi-Spectral Comparisons

3.2.1. Southern Hemisphere

Figure 10 shows a small section of the southern main auroral oval in the ultraviolet, infrared, and visible as observed by the Cassini spacecraft. These emissions are co-located in all three wavelength bands, to a very good approximation. This oval is directed poleward from -72° to -74° latitude and appears brightest between $\Psi_S = 320°$ and 330° in both the infrared and the ultraviolet. The two-dimensional distribution of the infrared auroral oval can be seen in Figure 4. The visible main oval appears more uniform in brightness, which is due to the fact that the projections average about an hour of visible images, as described in the previous section.

The spatial overlap of the main oval seen in the ultraviolet, infrared, and visible in Figure 10 is not perfect. For example, the infrared appears to have a slightly steeper latitude–longitude gradient than the ultraviolet and the visible. In Figure 10b the dashed, dot-dashed, and dot-dot-dot-dashed lines indicate the edge of the

FOV of each of the VIMS images seen in Figure 4, corresponding to Figures 4a, 4b, and 4c respectively. Across these edges, at 330° and 0° PPO longitude, there are distinct discontinuities in the H_3^+ emission. There is also emission at $\Psi_S =$ 350°, which is not seen in either the visible or the ultraviolet. These differences are not physical, and can be attributed to differences in the operational mode of the instruments, capturing glimpses of temporal and spatial variability at different times and locations. VIMS integrates a square FOV one pixel at a time, UVIS observes a single slit of emission at a time, and ISS integrates an entire square FOV at one time. Consequently, it becomes non-trivial to disentangle the spatial and temporal variability, especially when comparing morphology over a limited latitude and longitude region.

We do not expect there to be a difference in morphology between H Lyman-α in the ultraviolet and H Balmer-α in the visible, nor do we expect a difference between the ultraviolet H_2 and the visible H_2 emissions. However, there could be three principal reasons for differences between the observed H and H_2 emissions. Firstly, if the energy of the precipitating electrons is sufficiently low ($\sim$100s eV or less), only the very top of the upper atmosphere would be excited – the region dominated by atomic hydrogen. More broadly, highly tuned precipitation energies could produce significant differences between the H and H_2 morphologies. Secondly, atomic hydrogen emissions are subject to resonant scatter inside the atmosphere, producing a significantly more broad auroral emission, compared to that seen in molecular hydrogen. This effect is clearly seen in Figure 5. Thirdly, differences in how instruments acquire data can produce differences in the observed morphology, as discussed above.

At southern PPO longitudes of 0° to 20° in Figure 10 there is H_2 emission in the ultraviolet that is not seen in the visible observations, which capture a combination of H_2 and H Balmer-α emissions. This absence supports the notion that the ISS instrument is only able to capture the very brightest of the atomic hydrogen emission. This is corroborated by the relatively low S/N of the ISS images seen in Figures 6 and 10c. Alternatively, the bright H_2 emission at $\Psi_S = 20°$ longitude may not be contained within the ISS FOV or may not be simultaneous with the ISS observation.

The VIMS and UVIS instruments were acquiring data for a longer interval than ISS, and therefore they can be compared over a larger PPO longitude range. This is shown in Figure 12, covering 160° of PPO longitude, or about half of the PPO system, and 23° in latitude. These projections were constructed in the same manner as Figure 10. The main auroral emission are at similar latitudes in the two wavelength bands, with both showing the discontinuity at about $\Psi_S \simeq$330° and the kink at about 20°. There is a slight difference in the location of the discontinuity between the infrared and the ultraviolet, which is due to the two instruments observing it at different times. As noted, it is difficult to disentangle spatial and temporal variability due to differences in how these instruments operate. The brightest H_2 emission occurs at a longitude of $\sim$ 10°, which has no clear counterpart in the infrared H_3^+

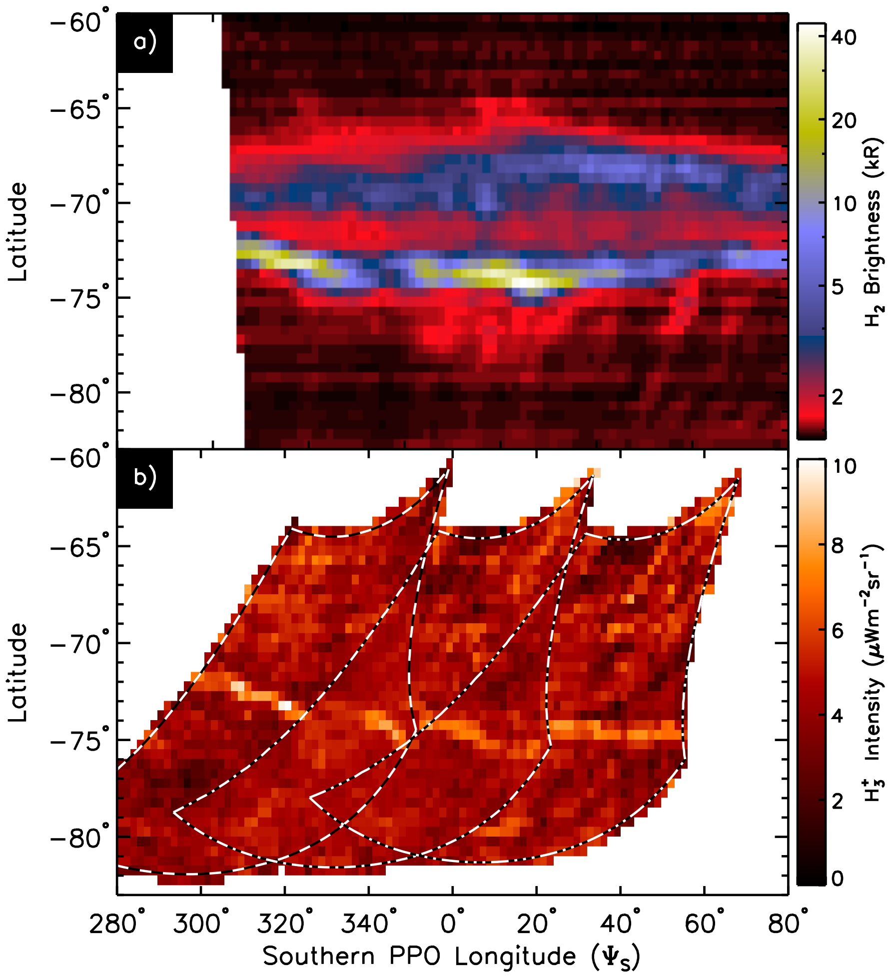

Figure 12: The a) ultraviolet UVIS H_2 Lyman and Werner bands and b) infrared VIMS H_3^+ auroral emissions near Saturn's southern pole on 2013-111, projected to latitude and longitude. The outline of each of the VIMS FOVs is shown as in Figure 10.

intensity. The brightest H_3^+ intensity occurs at about $\Psi_S = 320°$ PPO longitude, which agrees well with the second brightest H_2 emission.

The ultraviolet brightness scale in Figure 12a is exponential, whereas the infrared intensity scale in Figure 12b is linear. Therefore, the main oval is much more variable as seen in the ultraviolet, varying from a few kR to several tens of kR over spatial scales of a few of degrees longitude. The infrared main oval displays very limited variability, varying at the most by about 50% in intensity over the same spatial scales. The estimated energy flux of the precipitation is shown in Figure 5a. If one assumes that the ionospheric temperature does not vary over timescales of hours, as noted for the noon oval (O'Donoghue et al., 2014), the variability seen in Figure 12 is driven mainly by changes in the H_3^+ density. Thus, these observations broadly agree with the findings of Tao et al. (2011): the number density of H_3^+ is proportional to the square root of the precipitation energy flux.

The FOV of the HST observations, seen in Figure 7, does also include Saturn's southern pole. However, there is very little ultraviolet H_2 emission present there, having a S/N much too low to render it meaningful. By contrast, H_3^+ emission from the south is easily observed, as seen in Figure 9.

There is a fundamental difference between how auroral emissions are produced in the infrared and the ultraviolet in response to an injection of energy into the upper atmosphere (i.e. energetic electrons or solar photons). H_2 emits almost immediately after excitation, and is therefore an instantaneous view of the incoming source of energy. H_3^+, on the other hand, is produced by the chemical reaction described in Equation 1, becoming collisionally thermalized with the neutral atmosphere over the H_3^+ lifetime of up to 500 seconds (Melin et al., 2011a). This means that the H_3^+ emission maps the energy injection into the upper atmosphere over the duration of its lifetime, making it impossible to resolve temporal variability on timescales shorter than the H_3^+ lifetime. This also means that we are likely unable to observe very fine-scale variability like that seen in the ISS observations in Figure 6, even if an infrared observation were to have a spatial resolution of tens of km and very short integration times. The long lifetime of the ion would act as to produce a temporally averaged view over that lifetime. Additionally, since the H_3^+ ions are subject to transport, there are limitations on the minimum observable spatial resolution, which becomes a function of prevailing atmospheric dynamics. In contrast, the only effective limit on the temporal and spatial resolution of ultraviolet and visible observations is the integration time and spatial resolution of the instrumentation in question.

Figure 13 shows the dayside northern and southern intensity of the H_3^+ Q(1, 0^-) transition derived from the Keck and IRTF observations plotted versus UT time. The northern emission at midnight is subject to large line-of-sight effects and is excluded in this comparison. Also indicated is the total power emitted at the northern pole in the UV as observed by HST. At the top of the figure we show the northern (green) and southern (blue) PPO phases, indicated by arrows, with the expected locations of the maximum upward FACs indicated as an orthogonal solid line (as in Figure 4). It is important to note that all of the three instruments in Figure 13 have different FOVs, making comparisons between them not entirely straightforward. However, over the entire interval, between 09:00 UT and 13:00 UT, the infrared emissions from the northern pole observed with IRTF and Keck are broadly consistent with the HST observations which show very little variability about noon UT.

The HST images in Figure 7 clearly show an asymmetric auroral oval, emitting a near-constant power about noon UT. This is consistent with the Keck observations, but inconsistent with the IRTF observations which indicate a decrease in the east-west aligned H_3^+ intensity, likely driven by the uncertainty in pointing.

In examining the set of multispectral observations presented here, we must conclude that comparing like-for-like morphology in different wavelength bands is very challenging. The limitations created by the differences in how these instruments operate mean that even though these observations were obtained during the same interval, only a very small fraction represent emissions originating from the same point in time and space.

3.2.2. Northern Hemisphere

Figure 14 shows a comparison between the northern auroral emissions observed by the Earth-based platforms: HST, IRTF and Keck. Figures 14a and 14b show the background subtracted HST images, un-projected, as seen by the ACS instrument. Indicated on these panels are the width of the ground-based IRTF and Keck spectrograph slits. Panel c) shows the brightness of the part of the HST image that spatially overlaps the IRTF CSHELL slit, smoothed by $0.5''$ to simulate the atmospheric seeing that the ground-based facilities are subject to. Figure 14d shows the H_3^+ intensity as observed by IRTF CSHELL, quasi-simultaneous with the HST observations. This particular east-west comparison does not work well, as the IRTF observations suffered severe pointing errors. The IRTF profile in Figure 14d is much smeared in comparison to the HST profile in Figure 14c, rendering us to make any fruitful comments.

Figure 14e shows the mean HST brightness contained within the area that overlaps with the north-south aligned Keck slit, also smoothed by $0.5''$ to simulate the seeing produced by turbulence in Earth's atmosphere. The H_3^+ intensity seen by Keck is shown in Figure 14f. There is good correspondence between the infrared and ultraviolet emission above the terminator (above $z \simeq 0.6''$), as the emissions fall off with altitude above the planet, both being subject to near identical line-of-sight enhancements. This indicates that the H_2 and H_3^+ emissions are produced at similar altitudes in the atmosphere.

Below the terminator, however, on the body of the planet, there is a poor correspondence between the ultraviolet and infrared emissions. It is evident that the poleward emissions seen by the HST at noon are almost completely absent in the Keck observations. Since the intensity of H_3^+ is an exponential function of tem-

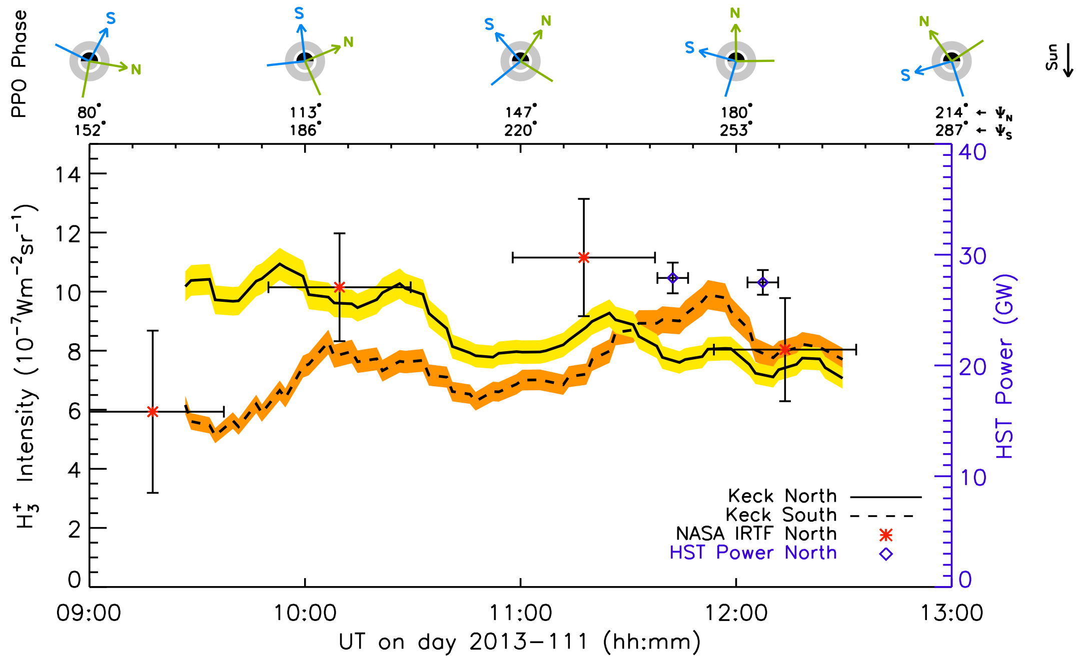

Figure 13: A qualitative comparison of the H_3^+ intensity of the northern and southern auroral polar regions as observed by Keck (solid and dotted lines, respectively, with the uncertainties shaded), the northern H_3^+ intensity as observed by the IRTF (stars), and the total power emitted in the ultraviolet as seen by HST in the north (diamonds). The schematics of Saturn along the top indicate the PPO phase, as in Figure 4. The northern and southern PPO phases are also given along the top axis.

perature (see Equation 2), a cool polar atmosphere would yield a very low infrared intensity radiated by each of the H_3^+ molecules produced by the precipitation process clearly seen in the ultraviolet. Indeed, O'Donoghue et al. (2015) showed that this region had a mean ionospheric temperature of 466±20 K, which makes H_3^+ a relatively poor emitter. Therefore, we conclude that the poleward emission is probably present in the H_3^+ emission, but the low temperature (and perhaps low density) of the ionopshere renders it invisible.

3.3. Auroral Brightness as a Function of PPO Phase

The correlation between the brightness of auroral emission and PPO phase has been noted by Nichols et al. (2010b), Badman et al. (2012b), and Lamy et al. (2013). Here, we investigate if there is a relationship present in the observations obtained in the interval considered here. We expect the peak upward FAC to be at $\Psi_N = 90°$ in the northern hemisphere and $\Psi_S = 270°$ in the southern hemisphere. These maxima are indicated in Figures 4, 6, 7, and 13 as solid lines at right angles to the arrows.

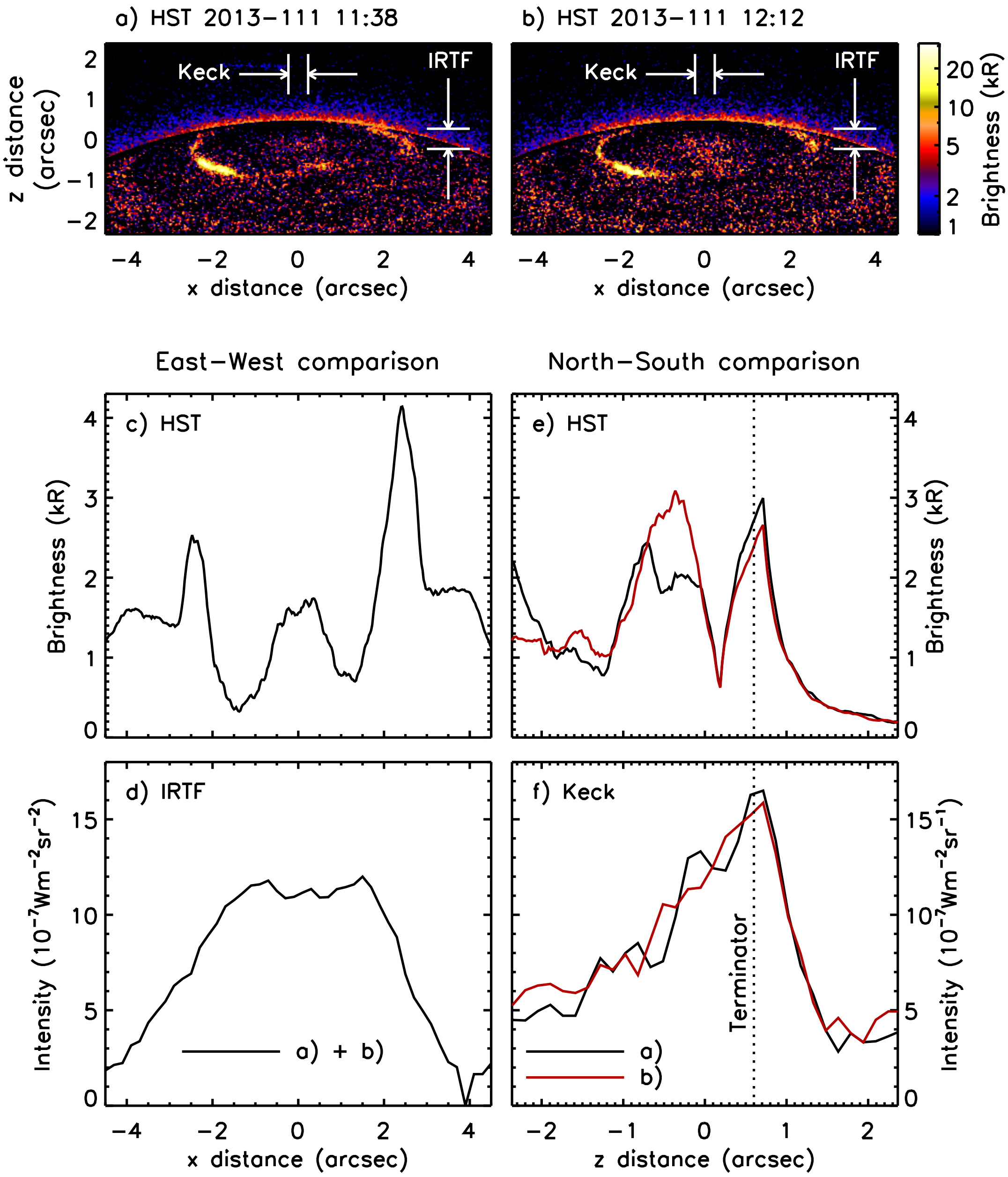

Figure 14: A comparison between simultaneous ultraviolet HST and infrared ground-based observations of Saturn's northern aurora. Panels a) and b) show the background subtracted northern auroral H_2 emissions as observed by HST, with the widths of the north-south aligned Keck NIRSPEC slit (0.46″) and east-west aligned IRTF CSHELL slit (0.5″) indicated. Panels c) and d) show a comparison between the east-west auroral brightness in the two wavelength bands and e) and f) contain the north-south comparison. The HST profiles are the average brightness contained within the respective ground-based spectrograph slit. There is emission present in the polar cap in the HST images that is absent in the infrared Keck observations. The IRTF observations suffered greatly from pointing errors, producing a very smeared profile.

By comparing the northern and southern PPO phase, $\Phi_{N,S}$, to the emissions detailed in this study (Figure 13, and others), we note the following for the emission observed through each instrument:

1. **HST:** The minimum FAC associated with the PPO current system is expected to be offset from the maximum by 180°. In the dawn sector in each of the four images in Figure 7 this region is markedly dimmer than regions just adjacent to it. Comparison of Figures 7c and 7d shows that the patch of aurora post-dusk is brightened as the peak upward FAC sweeps over this region.
2. **Keck:** In Figure 13, the peak northern upward FAC occurs at noon between 09:00 UT and 10:00 UT, $\Psi_N \simeq 100°$, as indicated by the green lines on the Saturn schematics. During this interval, the most intense northern H_3^+ emission is observed by Keck, which diminishes after 10:00 UT. The peak southern FAC occurs at about noon UT, $\Psi_S \simeq 260°$, which is close to where the most intense emission is observed from the southern aurora. Hence, both southern and northern H_3^+ emissions appear to be consistent with the expected intensity enhancements, governed by the prevailing PPO phase.
3. **IRTF:** The CHSELL slit is aligned east-west across the northern pole, and under optimal operational conditions we do not sample the H_3^+ emission present at either noon or midnight. When the upward northern FAC is located in the morning, there are no discernible dawn emissions (Figure 8a). However, when the maximum FAC has moved to the afternoon sector, the H_3^+ emission is markedly dusk brightened, seen in Figure 8f at 11:18 UT. Note that the brightness observed in the HST image obtained 20 minutes later, seen in Figure 7a, is significantly dawn brightened, which is inconsistent with the IRTF observations. The IRTF observations are not the ideal data-set for this comparison due to the extended period of observations to accrue sufficient S/N, with each image in Figure 8 covering about 23° of rotation, or 40 minutes. Both the telescope guiding errors and these long integrations are potential reasons for the inconsistencies between the IRTF and HST observations.
4. **VIMS:** In the LT projection of the VIMS observations in Figure 4, the FOV contains the direction of the azimuth of the southern PPO phase, $\Psi = 0°$. However, the three images do not contain either the maximum or minimum FAC associated with the PPO system, and therefore no fruitful examination can be performed.
5. **UVIS:** Figure 5 shows the ultraviolet emission observed as the planet rotates underneath the slit at a fixed 01:00 LT. The maximum upward FAC occurs in the south at $\Psi_S = 270°$, which is not captured by this sequence of UVIS exposures. The location of the minimum FAC at $\Psi_S = 90°$ deg passes under the UVIS slit at $\sim$12:30 UT and the brightness of the main oval decreased at this time compared to the adjacent times. The equatorward emission is at its brightest just prior to the arrival of the minimum FAC.

6. **ISS:** The very short interval during which ISS observed covers only a very limited range of PPO longitudes. This renders us unable to perform a meaningful comparison between emission brightness and PPO phase.

In the relatively short sequence of observations considered here, it is apparent that whilst the azimuth of the northern and southern maximum upward FAC associated with the PPO aligns reasonably with some auroral brightness features observed in this study, there are other features that do not.

3.4. Diffuse Equatorward Emissions

The UVIS observations in Figure 12a clearly show diffuse emission equatorward of the main oval, at a latitude of about -70°. In the southern hemisphere, this region maps to ∼8.8 R_S, whilst a latitude of -60° maps to ∼6.7 R_S (Burton et al., 2010). This location is broadly consistent with the equatorward emission observed by Grodent et al. (2010), which was associated with suprathermal electrons located between 4 and 11 R_S. It is also consistent with the arc seen in H_3^+ emission on the dawn and dusk side of the southern oval (Stallard et al., 2008), and with extended bands of H_3^+ emission seen on the southern dayside (Lamy et al., 2013). However, this equatorward band of emission seen by UVIS is notably absent in the infrared VIMS H_3^+ observations in Figure 12b. Such differences were previously noted by Melin et al. (2011a).

If there were a linear relationship between the H_2 and H_3^+ emission rates, then the equatorward emission would be observable in the infrared. Since this feature is not seen in Figure 12b, Equation 2 tells us that the differences in emission must be driven by temperature differences, producing exponential changes in the emission rate, and not differences in density, which result in linear changes. Assuming that the altitude of the peak emission rates of both H_3^+ and H_2 are very similar, as per Gérard et al. (2009) and Stallard et al. (2012), this suggests a steep temperature gradient decreasing towards the equator at this altitude.

We now calculate how much of a difference in ionospheric temperature is needed to produce the observed results. First, we assume that the excitation and ionization rate of H_2 are both linearly proportional to the UV brightness. With the equatorward H_2 emission being ∼4 times weaker than the main oval, we infer a ∼4 times difference in the H_3^+ production rate, and subsequently a ∼2 times difference in the H_3^+ density (i.e. $\sqrt{4}$; Tao et al., 2011). Secondly, if we consider Equation 2 for the H_3^+ Q(1, 0^-) transition, and assume that the auroral oval is at a temperature of about 450 K (Melin et al., 2007, 2011a; Lamy et al., 2013; O'Donoghue et al., 2014), then the diffuse equatorward auroral oval, separated by only a few degrees of latitude from the main oval, needs to be at a temperature of ∼400 K for it not to be observable, given a S/N of ∼5 of the observations in Figure 4. This rapid decrease in temperature with latitude, 50 K over 2-4°, is inconsistent with the UVIS occultation analysis of Koskinen et al. (2013), who measured a constant temperature near the exobase of ∼530 K, between latitudes of about -75° to -45°. In addition, we note that Lamy et al. (2013) observed equatorward emissions in both the infrared and the ultraviolet at the same time, which does not require the invocation of a steep temperature gradient equatorward of the main oval.

The steep temperature gradient implied by the VIMS and UVIS observations analysed here indicate that Joule heating in the main oval is substantially larger than seen in the equatorward band. Comparing this result to that of Lamy et al. (2013) suggests that the amount of Joule heating injected at sub-auroral latitudes is variable over time. The origin of the auroral signatures observed here is discussed below.

In Figure 15 we show the same types of H_3^+ intensity profiles and line-of-sight Doppler velocities as presented by Stallard et al. (2008), obtained by the same instrument, i.e. the CSHELL instrument on the IRTF. They found that after subtracting the modeled main oval emission at the southern pole, a band of equatorward emission was readily apparent. The distinct extended flanks on the dusk and dawn ansae that were seen by Stallard et al. (2008) are not seen in Figure 15. Hence, there is no evidence of dawn and dusk equatorward emission in the sunlit northern polar ionosphere. Additionally, in the HST images shown in Figure 7 there is no evidence of diffuse emission on the dayside at about 74° latitude. Since it is not seen on the dayside, during this interval, the FAC associated with this emission is confined to night-side local-times.

If the low latitude emission seen near the southern pole is related to the suprathermal population of electrons in the inner magnetosphere (Grodent et al., 2010), then we would expect this emission feature to be both conjugate and independent of local-time, since the inner regions of the magnetospheric plasma distribution are symmetric. These emissions are also unlikely to be associated with a secondary auroral oval (Stallard et al., 2008), as this also requires conjugacy and local-time independence. Mitchell et al. (2009a) suggested that field-aligned currents can be driven by pressure gradients associated with hot plasma regions in the middle magnetosphere. These emissions can be highly dependent on local-time, but they do require conjugacy. The presence of two upward FAC systems in the southern hemisphere agrees with the in-situ observations of Hunt et al. (2014), who observed the presence of both of these systems during most of the Cassini crossings of the open-closed field line boundary. Since the two current systems are present most of the time, they cannot be produced by intermittent ENAs. During the interval considered in this study, we have no observations of sub-auroral latitudes in the northern midnight sector, so it is not clear if there is a conjugate counterpart in the northern hemisphere to the equatorward diffuse emission in the southern.

The movement of the equatorward emission in Figure 5 indicates that the source of the associated FAC moves away from the planet until about 12:00 UT, after which it moves inward again. Whichever source is responsible for the equatorward emission, it must be able to account for both the motion and the H_2 intensity variability.

3.5. H_3^+ Ion Velocities

Figure 15 shows the H_3^+ intensity (solid) and velocity (dotted) for the intervals approximately coinciding with the HST images, derived using the CSHELL observations. In order to build up sufficient S/N, about two hours of data is co-added, averaging out any shorter-term variability shorter than these timescales. The figure shows the intensity and line-of-sight velocity of the H_3^+ emission at similar times to the first two and last two of the HST images in Figure 7, with the centre times of the IRTF observations shown. The solid line in Figure 15 is the intensity, the dotted is the line-of-sight velocity, and the dashed corresponds to rigid co-rotation assuming a period of 10.7 h. The shaded area indicates the region beyond the limb of the planet.

The integration times of the HST and IRTF observations are very different. In order to build up a good S/N in the velocity profile under the quiet conditions observed here, a rolling average of ~2 hours of observations needs to be co-added to produce the profiles in Figure 15. The HST observations, on the other hand, are only 500 s long. The HST images do not undergo dramatic brightness changes, in general agreement with the IRTF observations.

The H_3^+ ion velocities derived from the IRTF CSHELL data are affected by the extent to which accurate guiding of the telescope on the planet can be maintained. If the telescope moves significantly during the interval in question, velocities from different regions will be superimposed and the resulting structure becomes hard to interpret, as experienced during this interval. Here, the extent to which the telescope was able to maintain accurate guiding and track the planet across the sky is unclear.

The observations of Stallard et al. (2007a) suggest that a symmetric distribution of H_3^+ intensity across the polar cap, such as that shown in Figure 15, is associated with a three-region velocity structure. Here, the region just pre-noon that Stallard et al. (2007b) sees as co-rotating is being held at a zero velocity relative to rigid rotation (indicated as line 2 in Figure 15), and the region found by them to be sub-rotating at dawn is here approximately co-rotating (line 1). The sub-rotating region post-noon seen as line 3 in Figure 15a agrees well with the same region of Stallard et al. (2007b).

The east-west intensity profile of Figure 15a bears little resemblance to the dawn brightened morphology shown in the HST observations in Figures 7a and 7b. This means that either the CHSELL slit cuts along the line just above this brightening and thus misses it, or over a period of two hours the mean east-west profile averages out into something that is approximately symmetric about the pole. The pre-noon region of zero rotation in Figure 15a may be associated with a region linked to the solar wind, i.e. it is held in the inertial frame of the Sun. If the main auroral oval is associated with the open-closed field-line boundary (Bunce et al., 2008), then regions poleward of this are on field lines connecting to the solar wind.

Given the high degree of blending of velocities from different spatial regions across the pole, the velocities in Figure 15a are broadly consistent with a main oval that is sub-rotating, and a polar region that is being held by the solar wind at zero velocity, in the reference frame of the planet's atmosphere.

Figure 15b shows the velocity structure some 2 hours later, corresponding to the HST images of Figures 7c and 7d. Once again the large averaging produces a symmetric oval, with the bulk of the H_3^+ ions flowing at the co-rotation velocity. With the ions and neutrals flowing at a similar bulk velocity, we expect the collisional energy transferred between them to be at a minimum, and thus the auroral currents and emission intensity to be reduced. However, this is inconsistent with the HST observations that change very little over this interval, the total power varying only by a few percent. We attribute this discrepancy to the significant guiding error experienced at the IRTF.

3.6. Lessons for future Saturn auroral campaigns

Co-ordinating spacecraft and ground-based telescopes to observe the same object at the same time is notoriously hard. This is mainly because of scheduling issues, but as shown in this paper, the different temporal and spatial scales of different instruments introduce complexities that are difficult to disentangle. Each instrument has the potential to contribute a different story-line to the scientific narrative, and comparative studies can produce fruitful science (e.g. Lamy et al., 2013; Gérard et al., 2013). Hence, comparisons are possible, but care needs to be taken to understand the capabilities and limitations of each set of observations. If truly simultaneous comparisons between the VIMS and UVIS instruments are to be undertaken, and compared like for like, a more detailed analysis is available (Melin et al., 2011a), but this comes at the price of losing any two dimensional spatial information.

Here, we have only compared auroral morphologies observed in different wavelength bands obtained from different vantage points. This is but one of many ways in which to study this data. For example, no spectral analysis has been undertaken, which provides, amongst other things, a measure of the amount of energy injected into the upper atmosphere. As well, this study only uses infrared, visible, and ultraviolet remote sensing instruments. Cassini carries a whole host of others instruments with which comparisons can be made, including in-situ particle and fields instruments, radio, and ion/neutral imagers. This is to say that whilst it is non-trivial to compare simultaneous multi-wavelength morphologies, which can produce results that are inconsistent between data-sets, these types of observing campaigns facilitate science that is not possible with any one instrument. Therefore, the limitations in the analysis of morphology noted here does not mean that all types of comparisons will suffer in the same manner.

The observations analysed here were obtained during quiet solar wind conditions, resulting in a faint auroral oval. Therefore, the comparisons undertaken are at times limited by the S/N. The 2013 campaign covered about two months of observations,

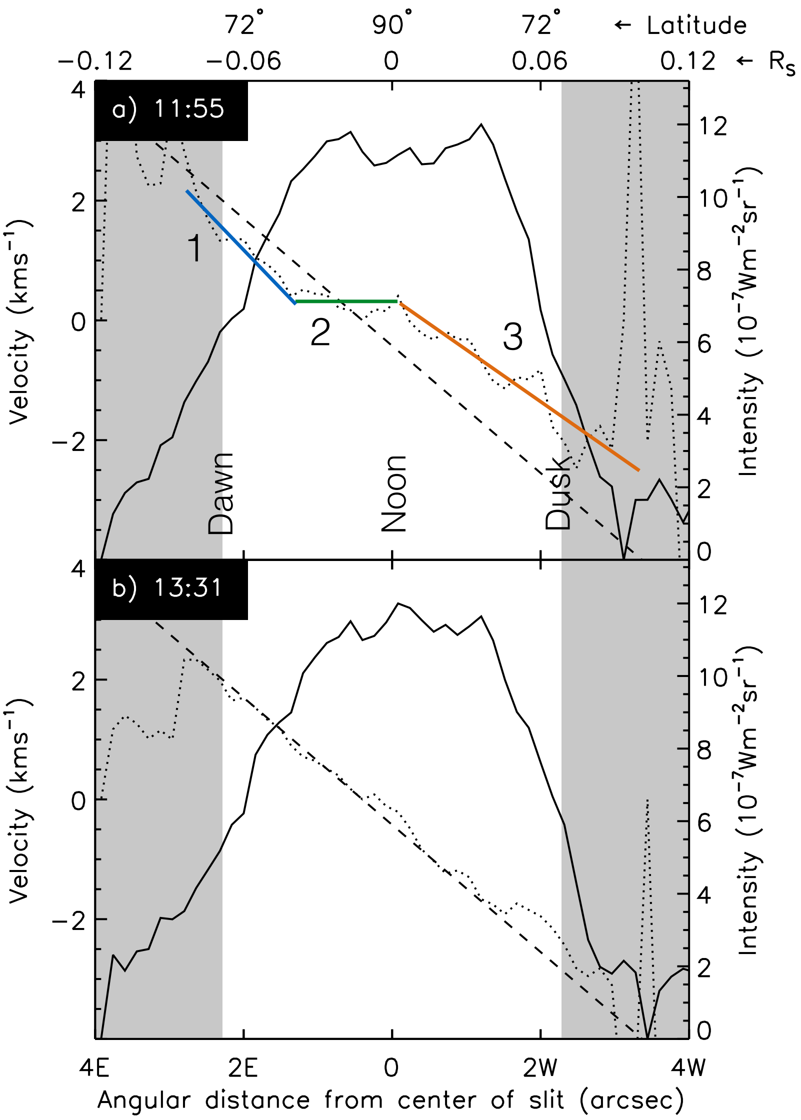

Figure 15: The H_3^+ ion intensity (solid) and velocity (dotted) derived from the IRTF CSHELL observations in Figure 8, for the intervals approximately centred on the times of the HST observations in Figure 7. The times indicate the mid-time for the interval for which data is co-added. The dashed line indicates the co-rotation velocity assuming a rotation period of 10.7 h, and the gray shaded areas indicate where the spectrograph slit is nominally outside the planet disk. Dusk is towards the right and dawn is towards the left. The three lines labelled 1, 2, and 3 show the distinct velocity regions discussed in Section 3.5. The two scales at the top indicate Saturn distance (R_S) and nominal latitude.

during which there were both active and quiet periods. It is imperative that future campaigns cover a similarly lengthy time-span, enabling us to observe a range of solar wind conditions, and how these relate to the observed emissions.

Observing campaigns that include ground-based data need to schedule enough of them so as to increase the probability of obtaining useful data, given the auroral S/N, weather, and telescope issues. These facilities are limited to observing during night-time hours at the Earth, and the other platforms, such as space telescopes and spacecraft, must take this into account.

4. Summary

We have compared the morphology of Saturn's aurora from six remote sensing instruments, all obtained on 21 April 2013, between 07:00 and 15:00 UT. These observations covered the infrared, visible, and ultraviolet, and included the NASA IRTF and Keck telescopes on the ground, the Hubble Space Telescope, and the Cassini spacecraft. The findings of these comparison can be summarised as follows:

1. These observations provide simultaneous multi-scale and multi-vantage-point views of the morphology of Saturn's auroral emissions. High spatial resolution Cassini ISS observations reveal spatial variability on several tens of km and brightness variability on timescales of minutes. Variability on larger spatial scales show that the total intensity of the oval varies not only over these short periods, but also over much longer timescales. This fine-structure variability seen inside the main oval is likely to be present at all times, as they are here clearly seen during a period of quiet auroral activity.
2. We directly compare the morphology of simultaneous infrared, visible, and ultraviolet auroral emissions. The main auroral emissions are approximately co-located in the midnight sector, forming an arc of width $\sim$0.5-1°, at 72-73° southern latitude, moving slightly equator-ward with increasing LT. The differences in morphology can be attributed to differences in how the instruments acquire their data, but may also be indicative of the fundamentally different emission mechanisms of excitation (H, H_2) and thermal emission via ionization of H_2 (H_3^+). The brightness of ultraviolet and visible main auroral emissions varies between $\sim$2 and 10 kR on timescales of 1-3 min and across spatial scales of $\sim$14-720 km on the planet. The intensity of the H_2 emissions varies by a factor of $\sim$10, from $\sim$4-40 kR, over timescales of 1 min and spatial scales of 720 km. The H_3^+ emissions vary less than the H_2 emissions, from $\sim$5-10 μW$m^2 sr^{-1}$, over similar spatial scales ($\sim$300 km) and timescales of a few seconds to a few hours.
3. The Keck observations of the H_3^+ intensity at local noon reveal a dependence on PPO phase which matches the predictions of auroral intensity related to FAC magnitude made by Provan et al. (2014), i.e. the northern H_3^+ intensity

is maximised at $\Psi_N \sim 90°$ and decreased until $\Psi_N > 180°$, while the southern intensity increased from $\Psi_S \sim 160°$ to a maximum around $\Psi_S \sim 250°$ (maxima are predicted at $\Psi_N \sim 90°$ and $\Psi_S \sim 270°$). Similarly, in the HST observations of the northern H_2 aurora, a post-dusk feature brightened as Ψ_N increased from $\sim$ 40 to 100°, i.e. as the region of expected maximum upward FAC rotated through this region. The nightside observations of H, H_2, and H_3^+ intensity also showed some dependence on PPO phase in that the intensity was greater at $\Psi_S \sim 300°$ than at $\Psi_S \sim 50°$.

4. Diffuse emissions equatorward of the main oval are only observed at the southern midnight sector in the ultraviolet using UVIS. The absence of these in the infrared H_3^+ emission suggests that this region is significantly cooler than the main auroral oval. We calculate that the required temperature difference is of the order of 50 K over 2-4° latitude. This emission is also not observed on the northern dayside by HST, showing that it is confined in local-time. This emission may be associated with the latitudinally separated FACs observed by Hunt et al. (2014), which are present at most times.
5. Our ability to perform like-for-like comparisons of multi-wavelength and multi-vantage point observations of Saturn's aurora is limited by a number of factors, such as auroral activity at Saturn, spacecraft instrument operational modes, weather on Earth, and accuracy of telescope guiding. With no ability to control all of those factors, future co-ordinated observing campaigns should aim to cover a long enough period, so as not to rely on a single interval or a single set of conditions.

Acknowledgments

Part of the data presented herein were obtained at the W.M. Keck Observatory, which is operated as a scientific partnership among the California Institute of Technology, the University of California and NASA. This work includes observations made with the NASA/ESA Hubble Space Telescope, obtained at the Space Telescope Science Institute, which is operated by AURA, Inc. for NASA. The observations were obtained during HST program GO 13051. HM, TSS, JO'D, JSDB, and REJ are visiting Astronomers at the Infrared Telescope Facility, which is operated by the University of Hawaii under Cooperative Agreement no. NNX-08AE38A with the NASA, Science Mission Directorate, Planetary Astronomy Program. This work was supported by the UK STFC Grant ST/K001000/1 for HM, TSS, SWHC, and GP, a Royal Astronomical Society Research Fellowship for SVB, and at SET by NASA CDAP grant NNX-13AG41G. JDN was supported by an STFC Advanced Fellowship. JO'D, JSDB, CJM, and REJ were supported by STFC studentships. JG is supported by the PRODEX program in collaboration with the Belgian Federal Science Policy Office (BELSPO). UD was supported by the NASA Cassini project. We thank G. M. Holsclaw for supplying the time-dependent UVIS calibration curves.

Appendix A. Instrumentation & Observations

The period of interest spans between 07:00 UT and 15:00 UT on 2013-111, which covers about three-quarters of a Saturn rotation. Figure 1 shows when each of the instruments were acquiring data. There is no time during which all of the six instruments were acquiring data, but between about 09:00 UT and 12:00 UT there are up to five instruments observing.

During the interval shown in Figure 1, Saturn was at a distance of 8.8 AU from the Earth (9.8 AU from the Sun), giving a light travel time of 4,403 s (1h 13m 23s). All the times in Figure 1 are adjusted to be UT at the time of emission at Saturn. This means that observations from Earth-based platforms are shifted backwards in time by the Earth-Saturn light travel time.

The observational geometry is shown in Figures 2 and 3. As viewed from the Earth, Saturn subtended 17″ pole-to-pole, having a right-ascension of α=14h 28m 09s and a declination δ=-11° 48m 18s. The planet reached a maximum elevation of 58° above the horizon (i.e. an airmass of 1.175) at 11:00 UT in Hawaii. Opposition of the Sun-Earth-Saturn system occurred on 28 April 2013.

What follows are brief outlines of the six instruments considered in this study.

Appendix A.1. Cassini Remote Sensing

The Visual and Infrared Mapping Spectrometer (VIMS, Brown et al., 2004), the Imaging Sub System Narrow Angle Camera (ISS, Porco et al., 2004), and the Ultraviolet Imaging Spectrograph (UVIS, Esposito et al., 2004) are mounted on the Cassini Remote Sensing Palette (RSP). These instruments share a common boresight, pointing along the `-y` direction, where the `+x` direction is along the stellar reference units, and `+z` is along the long axis that runs from the High Gain Antenna (HGA) towards the main rocket engines (Henry, 2002). The latitude and local-time projection of each of the fields of view of the Cassini instruments at 10:00 UT on 2013-111 can be seen in Figure 3.

During the observations considered here, Cassini was at a radial distance of 7 to 10 R_S from Saturn, in a 9.6 day orbit about the planet (orbit #187) with an orbital inclination of 62° from the equatorial plane. The spacecraft was located in the pre-midnight sector with a mean local-time of 22:49, and with a varying sub-Cassini latitude of -54° at 2013-111 07:00 UT and -34° at 2013-111 15:00 UT. The view of Saturn from Cassini during this interval can be seen in Figure 2a.

The pointing geometry of Cassini and its instrument boresights are derived from NASA's Navigation and Ancillary Information Facility (NAIF, Acton, 1996) in the usual manner. All the projections in latitude along one axis and either local-time, UT, or PPO longitude on the other axis are calculated at an altitude of 1100 km above the 1 bar reference surface. This is the altitude measured for both the peak intensity H_3^+ emission in the infrared (Stallard et al., 2012) and the peak brightness of the H_2 emission in the ultraviolet (Gérard et al., 2009). All latitudes are kronocentric and local-times are as given by NAIF, and the PPO phase is given by Provan et al. (2014). One degree of latitude represents ∼1000 km on the planet.

The Cassini pointing during this interval was approximately fixed in local-time, the geometry being shown in Figure 3. There is a slight drift in spacecraft pointing during this interval towards dawn, only readily apparent in the high spatial resolution observations of ISS (see Figure 6).

A single UVIS pixel contains 3 × 2 VIMS pixels, and a single VIMS pixel contains 83 × 83 ISS pixels. Because of the design and operational considerations of each instrument, combining these into truly simultaneous (i.e. emissions from the same place recorded at the same cadence) is non-trivial. Melin et al. (2011a) outline how simultaneous UVIS and VIMS observations can be combined to analyse auroral emissions at Saturn.

A brief outline of each of the Cassini instruments considered in this study follows below.

Appendix A.1.1. Cassini VIMS

VIMS has a field of view of 32 × 32 mrad, covering 64 × 64 pixels, with the instrument integrating each spatial pixel in sequence, so that no VIMS pixel is temporally simultaneous with any other. The spectral resolution is $R = \lambda/\Delta\lambda \sim 200$, and the total wavelength coverage is 0.8 to 5.1 µm, dispersed over 256 spectral pixels. This region includes discrete line emission of R and Q branch H_3^+ between 3.5 and 4.1 µm. See §2.9 in McCall (2001) for details of the H_3^+ spectroscopic notation used here.

We used the infrared bins 153, 155, 160, 165, 168, and 200 at 3.41, 3.44, 3.53, 3.61, 3.67, and 4.20 µm, respectively. The width of each wavelength bin is ∼0.017 µm. A background subtraction of the reflected solar light component is performed by subtracting the scaled intensity in wavelength bin 150 at 3.37 µm, in addition to subtraction of both the mean vertical and horizontal intensity profiles. This latter process acts to remove some of the systematic effects present in some wavelength bins. The integration time per pixel is 1 s, giving a total exposure time of 4160 s (including 64 dark current exposures). The diagonal bands seen at the top of the VIMS FOV in Figure 4c are due to instrumental effects sometimes present in a subset of wavelength bins, producing strips across the FOV. This behaviour is not well understood, and occurs only intermittently.

Appendix A.1.2. Cassini UVIS

The UVIS set of instruments has telescopes sensitive to both EUV and FUV wavelengths. Here, the FUV channel was used, which has a wavelength range of 112 to 191 nm dispersed over 1024 spectral elements and 64 spatial pixels along the slit, with a spectral resolution of $R \sim 500$. A spectral compression was used, producing a spectral image with 128 wavelength elements. Each individual spectrum was integrated for 60 s. The slit is 64 mrad long, and 1.5 pixels wide, with each pixel having a FOV of 1.5 × 1 mrad using the low-resolution slit, producing a mean spatial resolution on the planet of 720 km/pixel. The standard time-dependent University of Colorado calibration was applied to the UVIS data. The wavelength region of the UVIS FUV channel includes the Lyman and Werner H_2 band emissions, in addition to the H Lyman-α emission at 122 nm.

The UVIS FUV instrument has a relatively broad and complex line spread function (LSF) that disperses UV photons of a particular energy across the detector. This has to be accounted for when extracting the emission brightness of H and H_2. The H Lyman-α LSF is derived from observations of interplanetary hydrogen (IPH, i.e. a source of only Lyman-α) obtained during intervals when Cassini transfers data to the Earth via the Deep Space Network (DSN).

Appendix A.1.3. Cassini ISS

The ISS NAC is a $f/10.5$ Ritchey-Chretien telescope that has a square FOV with each side subtending 6.1 mrad, containing 1024 × 1024 pixels. It has a wavelength range of 0.2 to 1.05 µm, covering the visible part of the electromagnetic spectrum. In these observations the clear filter was used, covering 200 to 1050 nm, capturing auroral emission from H_2 and H Balmer-α at 0.66 µm, in addition to emission at other visible wavelengths. 37 ISS images were obtained between 08:40 UT and 10:38 UT, each 180 s long. A 4 × 4 spatial binning was used, giving a resolution per pixel on the planet of 14 km.

Observations of aurora in the visible wavelength region at Saturn are limited to nightside observations at a high phase angle, which makes the number of opportunities at which these observations are possible low, compared to auroral observations in the infrared or ultraviolet. These opportunities are strongly dependent on the spacecraft orbit.

Appendix A.2. Hubble Space Telescope ACS

The Advanced Camera for Surveys (ACS, Ford et al., 1998) is an ultraviolet-sensitive wide field 35×31″ (1024×1024 pixels) camera, installed on HST during Servicing Mission 3B in 2002. This spacecraft orbits with a period of ∼100 minutes, at a low-altitude Earth orbit.

Figure 7 shows four HST images, projected to latitude and local-time. Each exposure is 500 s, containing five co-adds of 100 s. The F125LP (CaF_2) filter was used, which has a maximum throughput at 130 nm, which excludes the bright H Lyman-α line. Hence, these observations purposefully exclude emissions that are associated with the geocorona of the Earth, a source of significant photon contamination. These observations were obtained on two consecutive HST Earth orbits, with images a) and b) being obtained at the beginning and at the end of a single orbit (and similarly for c and d). The noise floor in the HST images shown in Figure 7 is ∼2 kR.

Appendix A.3. NASA IRTF CSHELL

Located near the summit of Mauna Kea, Hawaii, at an altitude of 4,205 m above sea level, the NASA IRTF is a 3 m telescope equipped with the Cryogenic Echelle Spectrograph (CSHELL, Greene et al., 1993). This instrument provides a high spectral resolution of $R = \lambda/\Delta\lambda \sim 35000$, providing a theoretical velocity resolution of 3 km s^{-1}pixel^{-1}. The spatial extent along the slit is 30″, and the width is 0.5″. The spectral window was centered at the H_3^+ Q(1, 0^-) transition at 3.953 µm, and covered the region between 3.984 and 3.958 µm. The spectrograph slit was aligned east-west across the northern pole of Saturn, as indicated in Figure 2b. The observations presented here were reduced in the usual manner, using krypton and argon arc-lamps for wavelength calibration across the detector array. Half of the total integration time was spent on measurements of the prevailing Earth sky emissions (sky frames, or B frames), with the other half observing the polar region of Saturn (object frames, or A frames).

The largest source of uncertainty for the intensity shown in Figure 8 is inaccurate guiding of the telescope, which occurs from time to time. For these observations the guiding was particularly problematic, and the telescope could veer up off the planet, or down onto the planet. This occurs when there are no stars available for off-axis guiding and we are reliant only on using the tracking rates from the ephemeris. In the worst instances, telescope movements comparable to the size of the auroral region can occur on timescales of a single integration of 120 s. At the telescope, care is taken to note down the individual exposures subject to these movements so as to remove them from any subsquent analysis. Smaller movements are harder to discern, and may therefore still be present in the data presented here. Therefore, the error on both intensity, position, and derived velocities remain large, on the order of 30%. Under normal circumstances, data that is obtained during intervals with problematic guiding is not considered reliable, and is not used. It is included here because it adds another view of the Saturn system, but throughout the following analysis, we remind the reader that the errors are considerable, up to 2″.

It should be noted that Saturn's rings provide an excellent means by which to correct for guiding errors in long-slit spectra, since it provides a bright solar reflection spectrum with a fixed position relative to the aurora. This is always an available means if the slit is aligned north-south. If the slit is aligned east-west this method available about three years away from equinox, when the sub-observer latitude exceeds $\pm 25^{\circ}$, so that the tilt of the planet makes the rings and aurora appear along the same line-of-sight vector as seen from the Earth. This was not the case for the interval considered in this study.

By fitting the position of the spectral line in Figure 8 as a function of spectral and spatial position, the H_3^+ ion velocity can be derived, since emission from the ions is subject to Doppler shifts as they flow away or towards the Earth. This method was first applied to Jupiter (Rego et al., 1999; Stallard et al., 2001) and subsequently to Saturn (Stallard et al., 2007a). The uncertainty in the ion velocities is governed principally by the S/N and the accuracy of the telescope guiding: the S/N determines the accuracy to which the exact wavelength of the H_3^+ emission line can be determined at each spatial position and telescope guiding drifts produce a blending of emissions from different spatial positions. This is discussed further in Section 3.5.

Appendix A.4. Keck NIRSPEC

The 10 m twin Keck telescopes are located 235 m due West of the IRTF. On Keck II, the northernmost of the two telescopes, the Near Infrared Spectrograph (NIRSPEC, McLean et al., 1998) is mounted at one of the Nasmyth foci, providing near-infrared cross-dispersed spectra at a resolution of $R \sim 25{,}000$. When centred in the L band telluric atmospheric window, these emissions include both the R and Q branch of H_3^+. NIRSPEC has previously been used to study the ionosphere of Jupiter (Lystrup et al., 2008), Saturn (e.g. O'Donoghue et al., 2013), Uranus (Melin et al., 2011c), and Neptune (Melin et al., 2011b).

On 2013-111 Keck NIRSPEC observed Saturn for $\sim$3 h, as indicated in Figure 1. The $24''$ long slit was aligned parallel to the rotational axis, cutting through both the northern and southern auroral oval, traversing the rings. This geometry is shown in Figure 2b. The width of the spectrograph slit is $0.46''$, which is equivalent to about 1,400 km on the planet.

Spectral order 1 (of 4) of the NIRSPEC cross dispersed spectrum covered 3.95 to 4.00 µm, which includes part of the Q branch emission of H_3^+. Each exposure on the planet was 60 s and a sky exposure was obtained for each of these with equal exposure time. A total of 57 Saturn exposures were obtained, with the data being reduced in the normal manner, applying flat fields and dark frames. Flux calibration was achieved using observations of the A0 star HR 5717 (K magnitude 6.3).

References

Acton, C.H., 1996. Ancillary data services of NASA's Navigation and Ancillary Information Facility. Planetary and Space Science 44, 65–70. doi:10.1016/0032-0633(95)00107-7.

Aguilar, A., Ajello, J.M., Mangina, R.S., James, G.K., Abgrall, H., Roueff, E., 2008. The Electron-Excited Mid-Ultraviolet to Near-Infrared Spectrum of H_2: Cross Sections and Transition Probabilities. The Astrophysical Journal Supplement Series 177, 388–407. doi:10.1086/587690.

Andrews, D.J., Coates, A.J., Cowley, S.W.H., Dougherty, M.K., Lamy, L., Provan, G., Zarka, P., 2010. Magnetospheric period oscillations at Saturn: Comparison of equatorial and high-latitude magnetic field periods with north and south Saturn kilometric radiation periods. Journal of Geophysical Research (Space Physics) 115, 12252. doi:10.1029/2010JA015666.

Andrews, D.J., Cowley, S.W.H., Dougherty, M.K., Lamy, L., Provan, G., Southwood, D.J., 2012. Planetary period oscillations in Saturn's magnetosphere: Evolution of magnetic oscillation properties from southern summer to post-equinox. Journal of Geophysical Research (Space Physics) 117, 4224. doi:10.1029/2011JA017444.

Badman, S.V., Achilleos, N., Arridge, C.S., Baines, K.H., Brown, R.H., Bunce, E.J., Coates, A.J., Cowley, S.W.H., Dougherty, M.K., Fujimoto, M., Hospodarsky, G., Kasahara, S., Kimura, T., Melin, H., Mitchell, D.G., Stallard, T., Tao, C., 2012a. Cassini observations of ion and electron beams at Saturn and their relationship to infrared auroral arcs. Journal of Geophysical Research (Space Physics) 117, 1211. doi:10.1029/2011JA017222.

Badman, S.V., Achilleos, N., Baines, K.H., Brown, R.H., Bunce, E.J., Dougherty, M.K., Melin, H., Nichols, J.D., Stallard, T., 2011. Location of Saturn's northern infrared aurora determined from Cassini VIMS images. Geophysical Research Letters 38, 3102–+. doi:10.1029/2010GL046193.

Badman, S.V., Andrews, D.J., Cowley, S.W.H., Lamy, L., Provan, G., Tao, C., Kasahara, S., Kimura, T., Fujimoto, M., Melin, H., Stallard, T., Brown, R.H., Baines, K.H., 2012b. Rotational modulation and local time dependence of Saturn's infrared H_3^+ auroral intensity. Journal of Geophysical Research (Space Physics) 117, 9228. doi:10.1029/2012JA017990.

Badman, S.V., Branduardi-Raymont, G., Galand, M., Hess, S.L.G., Krupp, N., Lamy, L., Melin, H., Tao, C., 2014. Auroral Processes at the Giant Planets: Energy Deposition, Emission Mechanisms, Morphology and Spectra. Space Science Reviews doi:10.1007/s11214-014-0042-x.

Badman, S.V., Cowley, S.W.H., Gérard, J., Grodent, D., 2006. A statistical analysis of the location and width of Saturn's southern auroras. Annales Geophysicae 24, 3533–3545. doi:10.5194/angeo-24-3533-2006.

Badman, S.V., Masters, A., Hasegawa, H., Fujimoto, M., Radioti, A., Grodent, D., Sergis, N., Dougherty, M.K., Coates, A.J., 2013. Bursty magnetic reconnection at Saturn's magnetopause. Geophysical Research Letters 40, 1027–1031. doi:10.1002/grl.50199.

Belenkaya, E.S., Cowley, S.W.H., Nichols, J.D., Blokhina, M.S., Kalegaev, V.V., 2011. Magnetospheric mapping of the dayside UV auroral oval at Saturn using simultaneous HST images, Cassini IMF data, and a global magnetic field model. Annales Geophysicae 29, 1233–1246. doi:10.5194/angeo-29-1233-2011.

Bhardwaj, A., Gladstone, G.R., 2000. Auroral emissions of the giant planets. Reviews of Geophysics 38, 295–354. doi:10.1029/1998RG000046.

Brown, R.H., Baines, K.H., Bellucci, G., Bibring, J., Buratti, B.J., Capaccioni, F., Cerroni, P., Clark, R.N., Coradini, A., Cruikshank, D.P., Drossart, P., Formisano, V., Jaumann, R., Langevin, Y., Matson, D.L., McCord, T.B., Mennella, V., Miller, E., Nelson, R.M., Nicholson, P.D., Sicardy, B., Sotin, C., 2004. The Cassini Visual And Infrared Mapping Spectrometer (Vims) Investigation. Space Science Reviews 115, 111–168. doi:10.1007/s11214-004-1453-x.

Bunce, E.J., Arridge, C.S., Clarke, J.T., Coates, A.J., Cowley, S.W.H., Dougherty, M.K., Gérard, J., Grodent, D., Hansen, K.C., Nichols, J.D., Southwood, D.J., Talboys, D.L., 2008. Origin of Saturn's aurora: Simultaneous observations by Cassini and the Hubble Space Telescope. Journal of Geophysical Research (Space Physics) 113, 9209–+. doi:10.1029/2008JA013257.

Bunce, E.J., Grodent, D.C., Jinks, S.L., Andrews, D.J., Badman, S.V., Coates, A.J., Cowley, S.W.H., Dougherty, M.K., Kurth, W.S., Mitchell, D.G., Provan, G., 2014. Cassini nightside observations of the oscillatory motion of Saturn's northern auroral oval. Journal of Geophysical Research (Space Physics) 119, 3528–3543. doi:10.1002/2013JA019527.

Burton, M.E., Dougherty, M.K., Russell, C.T., 2010. Saturn's internal planetary magnetic field. Geophysical Research Letters 37, 24105. doi:10.1029/2010GL045148.

Carbary, J.F., Mitchell, D.G., Brandt, P., Roelof, E.C., Krimigis, S.M., 2008. Statistical morphology of ENA emissions at Saturn. Journal of Geophysical Research (Space Physics) 113, 5210. doi:10.1029/2007JA012873.

Carbary, J.F., Mitchell, D.G., Krimigis, S.M., Krupp, N., 2009. Dual periodicities in energetic electrons at Saturn. Geophysical Research Letters 36, 20103. doi:10.1029/2009GL040517.

Clarke, J.T., Nichols, J., Gérard, J.C., Grodent, D., Hansen, K.C., Kurth, W., Gladstone, G.R., Duval, J., Wannawichian, S., Bunce, E., Cowley, S.W.H., Crary, F., Dougherty, M., Lamy, L., Mitchell, D., Pryor, W., Retherford, K., Stallard, T., Zieger, B., Zarka, P., Cecconi, B., 2009. Response of Jupiter's and Saturn's auroral activity to the solar wind. Journal of Geophysical Research (Space Physics) 114, 5210. doi:10.1029/2008JA013694.

Connerney, J.E.P., Waite, J.H., 1984. New model of Saturn's ionosphere with an influx of water from the rings. Nature 312, 136–138. doi:10.1038/312136a0.

Cowley, S., Bunce, E., Prangé, R., 2004. Saturn's polar ionospheric flows and their relation to the main auroral oval. Annales Geophysicae 22, 1379–1394. doi:10.5194/angeo-22-1379-2004.

Cowley, S.W.H., Badman, S.V., Bunce, E.J., Clarke, J.T., GéRard, J.C., Grodent, D., Jackman, C.M., Milan, S.E., Yeoman, T.K., 2005. Reconnection in a rotation-dominated magnetosphere and its relation to Saturn's auroral dynamics. Journal of Geophysical Research (Space Physics) 110, 2201. doi:10.1029/2004JA010796.

Crary, F.J., Clarke, J.T., Dougherty, M.K., Hanlon, P.G., Hansen, K.C., Steinberg, J.T., Barraclough, B.L., Coates, A.J., Gérard, J.C., Grodent, D., Kurth, W.S., Mitchell, D.G., Rymer, A.M., Young, D.T., 2005. Solar wind dynamic pressure and electric field as the main factors controlling Saturn's aurorae. Nature 433, 720–722. doi:10.1038/nature03333.

Espinosa, S.A., Dougherty, M.K., 2000. Periodic perturbations in Saturn's magnetic field. Geophysical Research Letters 27, 2785–2788. doi:10.1029/2000GL000048.

Esposito, L.W., Barth, C.A., Colwell, J.E., Lawrence, G.M., McClintock, W.E., Stewart, A.I.F., Keller, H.U., Korth, A., Lauche, H., Festou, M.C., Lane, A.L., Hansen, C.J., Maki, J.N., West, R.A., Jahn, H., Reulke, R., Warlich, K., Shemansky, D.E., Yung, Y.L., 2004. The Cassini Ultraviolet Imaging Spectrograph Investigation. Space Science Reviews 115, 299–361. doi:10.1007/s11214-004-1455-8.

Ford, H.C., Bartko, F., Bely, P.Y., Broadhurst, T., Burrows, C.J., Cheng, E.S., Clampin, M., Crocker, J.H., Feldman, P.D., Golimowski, D.A., Hartig, G.F., Illingworth, G., Kimble, R.A., Lesser, M.P., Miley, G., Neff, S.G., Postman, M., Sparks, W.B., Tsvetanov, Z., White, R.L., Sullivan, P., Krebs, C.A., Leviton, D.B., La Jeunesse, T., Burmester, W., Fike, S., Johnson, R., Slusher, R.B., Volmer, P., Woodruff, R.A., 1998. Advanced camera for the Hubble Space Telescope, in: Bely, P.Y., Breckinridge, J.B. (Eds.), Space Telescopes and Instruments V, pp. 234–248.

Galopeau, P.H.M., Lecacheux, A., 2000. Variations of Saturn's radio rotation period measured at kilometer wavelengths. Journal of Geophysical Research 105, 13089–13102. doi:10.1029/1999JA005089.

Geballe, T.R., Jagod, M., Oka, T., 1993. Detection of H_3^+ infrared emission lines in Saturn. Astrophysical Journal Letters 408, L109–L112. doi:10.1086/186843.

Gérard, J., Bonfond, B., Gustin, J., Grodent, D., Clarke, J.T., Bisikalo, D., Shematovich, V., 2009. Altitude of Saturn's aurora and its implications for the characteristic energy of precipitated electrons. Geophysical Research Letters 36, L02202. doi:10.1029/2008GL036554.

Gérard, J.C., Bunce, E.J., Grodent, D., Cowley, S.W.H., Clarke, J.T., Badman, S.V., 2005. Signature of Saturn's auroral cusp: Simultaneous Hubble Space Telescope FUV observations and upstream solar wind monitoring. Journal of Geophysical Research (Space Physics) 110, 11201. doi:10.1029/2005JA011094.

Gérard, J.C., Grodent, D., Cowley, S.W.H., Mitchell, D.G., Kurth, W.S., Clarke, J.T., Bunce, E.J., Nichols, J.D., Dougherty, M.K., Crary, F.J., Coates, A.J., 2006. Saturn's auroral morphology and activity during quiet magnetospheric conditions. Journal of Geophysical Research (Space Physics) 111, 12210. doi:10.1029/2006JA011965.

Gérard, J.C., Gustin, J., Pryor, W.R., Grodent, D., Bonfond, B., Radioti, A., Gladstone, G.R., Clarke, J.T., Nichols, J.D., 2013. Remote sensing of the energy of auroral electrons in Saturn's atmosphere: Hubble and Cassini spectral observations. Icarus 223, 211–221. doi:10.1016/j.icarus.2012.11.033.

Goldreich, P., Farmer, A.J., 2007. Spontaneous axisymmetry breaking of the external magnetic field at Saturn. Journal of Geophysical Research (Space Physics) 112, 5225. doi:10.1029/2006JA012163, arXiv:astro-ph/0608296.

Greene, T.P., Tokunaga, A.T., Toomey, D.W., Carr, J.B., 1993. CSHELL: a high spectral resolution 1-5 um cryogenic echelle spectrograph for the IRTF, in: Fowler, A.M. (Ed.), Infrared Detectors and Instrumentation, pp. 313–324.

Grodent, D., Radioti, A., Bonfond, B., Gérard, J., 2010. On the origin of Saturn's outer auroral emission. Journal of Geophysical Research (Space Physics) 115, 8219–+. doi:10.1029/2009JA014901.

Gurnett, D.A., Lecacheux, A., Kurth, W.S., Persoon, A.M., Groene, J.B., Lamy, L., Zarka, P., Carbary, J.F., 2009. Discovery of a north-south asymmetry in Saturn's radio rotation period. Geophysical Research Letters 36, 16102. doi:10.1029/2009GL039621.

Gustin, J., Bonfond, B., Grodent, D., Gérard, J.C., 2012. Conversion from HST ACS and STIS auroral counts into brightness, precipitated power, and radiated power for H_2 giant planets. Journal of Geophysical Research (Space Physics) 117, 7316. doi:10.1029/2012JA017607.

Gustin, J., Gérard, J., Pryor, W., Feldman, P.D., Grodent, D., Holsclaw, G., 2009. Characteristics of Saturn's polar atmosphere and auroral electrons derived from HST/STIS, FUSE and Cassini/UVIS spectra. Icarus 200, 176–187. doi:10.1016/j.icarus.2008.11.013.

Gustin, J., Gérard, J.C., Grodent, D., Gladstone, G.R., Clarke, J.T., Pryor, W.R., Dols, V., Bonfond, B., Radioti, A., Lamy, L., Ajello, J.M., 2013. Effects of methane on giant planet's UV emissions and implications for the auroral characteristics. Journal of Molecular Spectroscopy 291, 108–117. doi:10.1016/j.jms.2013.03.010.

Henry, C.A., 2002. An Introduction to the Design of the Cassini Spacecraft. Space Science Reviews 104, 129–153. doi:10.1023/A:1023696808894.

Hunt, G.J., Cowley, S.W.H., Provan, G., Bunce, E.J., Alexeev, I.I., Belenkaya, E.S., Kalegaev, V.V., Dougherty, M.K., Coates, A.J., 2014. Field-aligned currents in Saturn's southern nightside magnetosphere: Subcorotation and planetary period oscillation components. Journal of Geophysical Research (Space Physics) 119, 9847–9899. doi:10.1002/2014JA020506.

Jia, X., Kivelson, M.G., Gombosi, T.I., 2012. Driving Saturn's magnetospheric periodicities from the upper atmosphere/ionosphere. Journal of Geophysical Research (Space Physics) 117, 4215. doi:10.1029/2011JA017367.

Klimas, A., Uritsky, V., Donovan, E., 2010. Multiscale auroral emission statistics as evidence of turbulent reconnection in Earth's midtail plasma sheet. Journal of Geophysical Research (Space Physics) 115, 6202. doi:10.1029/2009JA014995.

Koskinen, T.T., Sandel, B.R., Yelle, R.V., Capalbo, F.J., Holsclaw, G.M., McClintock, W.E., Edgington, S., 2013. The density and temperature structure near the exobase of Saturn from Cassini UVIS solar occultations. Icarus 226, 1318–1330. doi:10.1016/j.icarus.2013.07.037.

Kurth, W.S., Bunce, E.J., Clarke, J.T., Crary, F.J., Grodent, D.C., Ingersoll, A.P., Dyudina, U.A., Lamy, L., Mitchell, D.G., Persoon, A.M., Pryor, W.R., Saur, J., Stallard, T., 2009. Saturn from Cassini-Huygens. Springer. chapter Auroral Processes. p. 333.

Lamy, L., Cecconi, B., Prangé, R., Zarka, P., Nichols, J.D., Clarke, J.T., 2009. An auroral oval at the footprint of Saturn's kilometric radio sources, colocated with the UV aurorae. Journal of Geophysical Research (Space Physics) 114, A10212. doi:10.1029/2009JA014401.

Lamy, L., Cecconi, B., Zarka, P., Canu, P., Schippers, P., Kurth, W.S., Mutel, R.L., Gurnett, D.A., Menietti, D., Louarn, P., 2011. Emission and propagation of Saturn kilometric radiation: Magnetoionic modes, beaming pattern, and polarization state. Journal of Geophysical Research (Space Physics) 116, 4212. doi:10.1029/2010JA016195, arXiv:1101.3666.

Lamy, L., Prangé, R., Pryor, W., Gustin, J., Badman, S.V., Melin, H., Stallard, T., Mitchell, D.G., Brandt, P.C., 2013. Multispectral simultaneous diagnosis of Saturn's aurorae throughout a planetary rotation. Journal of Geophysical Research (Space Physics) 118, 4817–4843. doi:10.1002/jgra.50404, arXiv:1307.4675.

Lystrup, M.B., Miller, S., Dello Russo, N., Vervack, Jr., R.J., Stallard, T., 2008. First Vertical Ion Density Profile in Jupiter's Auroral Atmosphere: Direct Observations using the Keck II Telescope. Astrophysical Journal 677, 790–797. doi:10.1086/529509.

McCall, B.J., 2001. Spectroscopy of trihydrogen(+) in laboratory and astrophysical plasmas. Ph.D. thesis. Department of Chemistry and Department of Astronomy and Astrophysics, University of Chicago.

McLean, I.S., Becklin, E.E., Bendiksen, O., Brims, G., Canfield, J., Figer, D.F., Graham, J.R., Hare, J., Lacayanga, F., Larkin, J.E., Larson, S.B., Levenson, N., Magnone, N., Teplitz, H., Wong, W., 1998. Design and development of NIRSPEC: a near-infrared echelle spectrograph for the Keck II telescope, in: A. M. Fowler (Ed.), Society of Photo-Optical Instrumentation Engineers (SPIE) Conference Series, pp. 566–578.

Melin, H., Miller, S., Stallard, T., Trafton, L.M., Geballe, T.R., 2007. Variability in the H_3^+ emission of Saturn: Consequences for ionisation rates and temperature. Icarus 186, 234–241. doi:10.1016/j.icarus.2006.08.014.

Melin, H., Stallard, T., Miller, S., Gustin, J., Galand, M., Badman, S.V., Pryor, W.R., O'Donoghue, J., Brown, R.H., Baines, K.H., 2011a. Simultaneous Cassini VIMS and UVIS observations of Saturn's southern aurora: Comparing emissions from H, H_2 and $H_3{}^+$ at a high spatial resolution. Geophysical Research Letters 381, L15203. doi:10.1029/2011GL048457.

Melin, H., Stallard, T., Miller, S., Lystrup, M.B., Trafton, L.M., Booth, T.C., Rivers, C., 2011b. New limits on $H^+{}_3$ abundance on Neptune using Keck NIRSPEC. MNRAS 410, 641–644. doi:10.1111/j.1365-2966.2010.17468.x.

Melin, H., Stallard, T., Miller, S., Trafton, L.M., Encrenaz, T., Geballe, T.R., 2011c. Seasonal Variability in the Ionosphere of Uranus. The Astronomical Journal 729, 134. doi:10.1088/0004-637X/729/2/134.

Menager, H., Barthélemy, M., Lilensten, J., 2010. H Lyman α line in Jovian aurorae: electron transport and radiative transfer coupled modelling. Astronomy and Astrophysics 509, A56. doi:10.1051/0004-6361/200912952.

Meredith, C.J., Alexeev, I.I., Badman, S.V., Belenkaya, E.S., Cowley, S.W.H., Dougherty, M.K., Kalegaev, V.V., Lewis, G.R., Nichols, J.D., 2014. Saturn's dayside ultraviolet auroras: Evidence for morphological dependence on the direction of the upstream interplanetary magnetic field. Journal of Geophysical Research (Space Physics) 119, 1994–2008. doi:10.1002/2013JA019598.

Miller, S., Stallard, T., Tennyson, J., Melin, H., 2013. Cooling by H_3^+ Emission. Journal of Physical Chemistry A 117, 9770–9777. doi:10.1021/jp312468b.

Mitchell, D.G., Krimigis, S.M., Paranicas, C., Brandt, P.C., Carbary, J.F., Roelof, E.C., Kurth, W.S., Gurnett, D.A., Clarke, J.T., Nichols, J.D., Gérard, J.C., Grodent, D.C., Dougherty, M.K., Pryor, W.R., 2009a. Recurrent energization of plasma in the midnight-to-dawn quadrant of Saturn's magnetosphere, and its relationship to auroral UV and radio emissions. Planetary and Space Science 57, 1732–1742. doi:10.1016/j.pss.2009.04.002.

Mitchell, D.G., Kurth, W.S., Hospodarsky, G.B., Krupp, N., Saur, J., Mauk, B.H., Carbary, J.F., Krimigis, S.M., Dougherty, M.K., Hamilton, D.C., 2009b. Ion conics and electron beams associated with auroral processes on Saturn. Journal of Geophysical Research (Space Physics) 114, A02212. doi:10.1029/2008JA013621.

Neale, L., Miller, S., Tennyson, J., 1996. Spectroscopic Properties of the H_3^+ Molecule: A New Calculated Line List. Astrophysical Journal 464, 516–+. doi:10.1086/177341.

Nichols, J.D., Badman, S.V., Baines, K.H., Brown, R.H., Bunce, E.J., Clarke, J.T., Cowley, S.W.H., Crary, F.J., Dougherty, M.K., Gérard, J.C., Grocott, A., Grodent, D., Kurth, W.S., Melin, H., Mitchell, D.G., Pryor, W.R., Stallard, T.S., 2014. Dynamic auroral storms on Saturn as observed by the Hubble Space Telescope. Geophysical Research Letters 41, 3323–3330. doi:10.1002/2014GL060186.

Nichols, J.D., Cecconi, B., Clarke, J.T., Cowley, S.W.H., Gérard, J.C., Grocott, A., Grodent, D., Lamy, L., Zarka, P., 2010a. Variation of Saturn's UV aurora with SKR phase. Geophysical Research Letters 37, 15102. doi:10.1029/2010GL044057.

Nichols, J.D., Cowley, S.W.H., Lamy, L., 2010b. Dawn-dusk oscillation of Saturn's conjugate auroral ovals. Geophysical Research Letters 37, 24102. doi:10.1029/2010GL045818.

O'Donoghue, J., Melin, H., Stallard, T.S., Provan, G., Moore, L., Badman, S.V., Cowley, S.W.H., Baines, K.H., Miller, S., Blake, J.S.D., 2015. Ground-based observations of Saturn's auroral ionosphere over three days: Trends in H_3^+ temperature, density and emission with Saturn local time and planetary period oscillation. Icarus *in press* doi:doi:10.1016/j.icarus.2015.04.018.

O'Donoghue, J., Stallard, T.S., Melin, H., Cowley, S.W.H., Badman, S.V., Moore, L., Miller, S., Tao, C., Baines, K.H., Blake, J.S.D., 2014. Conjugate observations of Saturn's northern and southern H_3^+ aurorae. Icarus 229, 214–220. doi:10.1016/j.icarus.2013.11.009, arXiv:1311.1927.

O'Donoghue, J., Stallard, T.S., Melin, H., Jones, G.H., Cowley, S.W.H., Miller, S., Baines, K.H., Blake, J.S.D., 2013. The domination of Saturn's low-latitude ionosphere by ring 'rain'. Nature 496, 193–195. doi:10.1038/nature12049.

Porco, C.C., West, R.A., Squyres, S., McEwen, A., Thomas, P., Murray, C.D., Del Genio, A., Ingersoll, A.P., Johnson, T.V., Neukum, G., Veverka, J., Dones, L., Brahic, A., Burns, J.A., Haemmerle, V., Knowles, B., Dawson, D., Roatsch, T., Beurle, K., Owen, W., 2004. Cassini Imaging Science: Instrument Characteristics And Anticipated Scientific Investigations At Saturn. Space Science Reviews 115, 363–497. doi:10.1007/s11214-004-1456-7.

Prangé, R., Fouchet, T., Courtin, R., Connerney, J.E.P., McConnell, J.C., 2006. Latitudinal variation of Saturn photochemistry deduced from spatially-resolved ultraviolet spectra. Icarus 180, 379–392. doi:10.1016/j.icarus.2005.11.005.

Provan, G., Cowley, S.W.H., Nichols, J.D., 2009. Phase relation of oscillations near the planetary period of Saturn's auroral oval and the equatorial magnetospheric magnetic field. Journal of Geophysical Research (Space Physics) 114, 4205. doi:10.1029/2008JA013988.

Provan, G., Lamy, L., Cowley, S.W.H., Dougherty, M.K., 2014. Planetary period oscillations in Saturn's magnetosphere: Comparison of magnetic oscillations and SKR modulations in the postequinox interval. Journal of Geophysical Research (Space Physics) 119, 7380–7401. doi:10.1002/2014JA020011.

Radioti, A., Grodent, D., Gérard, J.C., Milan, S.E., Bonfond, B., Gustin, J., Pryor, W., 2011. Bifurcations of the main auroral ring at Saturn: ionospheric signatures of consecutive reconnection events at the magnetopause. Journal of Geophysical Research (Space Physics) 116, 11209. doi:10.1029/2011JA016661.

Rego, D., Achilleos, N., Stallard, T., Miller, S., Prangé, R., Dougherty, M., Joseph, R.D., 1999. Supersonic winds in Jupiter's aurorae. Nature 399, 121–124. doi:10.1038/20121.

Shemansky, D.E., Ajello, J.M., 1983. The Saturn spectrum in the EUV - Electron excited hydrogen. Journal of Geophysical Research 88, 459–464. doi:10.1029/JA088iA01p00459.

Smith, C.G.A., 2006. Periodic modulation of gas giant magnetospheres by the neutral upper atmosphere. Annales Geophysicae 24, 2709–2717. doi:10.5194/angeo-24-2709-2006.

Smith, C.G.A., 2014. On the nature and location of the proposed twin vortex systems in Saturn's polar upper atmosphere. Journal of Geophysical Research (Space Physics) 119, 5964–5977. doi:10.1002/2014JA019934.

Southwood, D.J., Cowley, S.W.H., 2014. The origin of Saturn's magnetic periodicities: Northern and southern current systems. Journal of Geophysical Research (Space Physics) 119, 1563–1571. doi:10.1002/2013JA019632.

Southwood, D.J., Kivelson, M.G., 2007. Saturnian magnetospheric dynamics: Elucidation of a camshaft model. Journal of Geophysical Research (Space Physics) 112, 12222. doi:10.1029/2007JA012254.

Stallard, T., Miller, S., Melin, H., Lystrup, M., Cowley, S.W.H., Bunce, E.J., Achilleos, N., Dougherty, M., 2008. Jovian-like aurorae on Saturn. Nature 453, 1083–1085. doi:10.1038/nature07077.

Stallard, T., Miller, S., Melin, H., Lystrup, M., Dougherty, M., Achilleos, N., 2007a. Saturn's auroral/polar ${H^+}_3$ infrared emission. I. General morphology and ion velocity structure. Icarus 189, 1–13. doi:10.1016/j.icarus.2006.12.027.

Stallard, T., Miller, S., Millward, G., Joseph, R.D., 2001. On the Dynamics of the Jovian Ionosphere and Thermosphere. I. The Measurement of Ion Winds. Icarus 154, 475–491. doi:10.1006/icar.2001.6681.

Stallard, T., Smith, C., Miller, S., Melin, H., Lystrup, M., Aylward, A., Achilleos, N., Dougherty, M., 2007b. Saturn's auroral/polar H_3^+ infrared emission. II. A comparison with plasma flow models. Icarus 191, 678–690. doi:10.1016/j.icarus.2007.05.016.

Stallard, T.S., Melin, H., Miller, S., Badman, S.V., Brown, R.H., Baines, K.H., 2012. Peak emission altitude of Saturn's ${H_3}^+$ aurora. Geophysical Research Letters 39, 15103. doi:10.1029/2012GL052806.

Talboys, D.L., Arridge, C.S., Bunce, E.J., Coates, A.J., Cowley, S.W.H., Dougherty, M.K., 2009. Characterization of auroral current systems in Saturn's magnetosphere: High-latitude Cassini observations. Journal of Geophysical Research (Space Physics) 114, A06220. doi:10.1029/2008JA013846.

Tao, C., Badman, S.V., Fujimoto, M., 2011. UV and IR auroral emission model for the outer planets: Jupiter and Saturn comparison. Icarus 213, 581–592. doi:10.1016/j.icarus.2011.04.001.

Uritsky, V.M., Donovan, E., Trondsen, T., Pineau, D., Kozelov, B.V., 2010. Data-derived spatiotemporal resolution constraints for global auroral imagers. Journal of Geophysical Research (Space Physics) 115, 9205. doi:10.1029/2010JA015365.

Weiser, H., Vitz, R.C., Moos, H.W., 1977. Detection of Lyman-alpha emission from the Saturnian disk and from the ring system. Science 197, 755–757. doi:10.1126/science.197.4305.755.